Functional recycling of grain boundary diffusion processed Nd-Fe-B sintered magnets

Mario Schönfeldt [a,b,*], Jürgen Rossa [a], Konrad Opelt [a,b], Kilian Schäfer [b], Lukas Schäfer [b], Fernando Maccari [b], Matic Jovičević-Klug [c], Tim M. Schwarz [c], Chi-Chia Lin [a,b], Mahmudul Hasan [a], Jürgen Gassmann [a], Dierk Raabe [c], Oliver Gutfleisch [b]

[a] Fraunhofer IWKS, Fraunhofer Research Institution for Materials Recycling and Resource Strategies, Aschaffenburger Str. 121, 63457 Hanau, Germany
[b] TU Darmstadt, Department of Materials and Geosciences, Functional Materials, Peter-Grünberg-Str. 16, 64287 Darmstadt, Germany
[c] Max-Planck-Institute for Sustainable Materials GmbH, Department of Microstructure Physics and Alloy Design, Max-Planck-Str. 1, 40237 Düsseldorf, Germany

ARTICLE INFO

ABSTRACT

Sintered Nd-Fe-B magnets industrially produced employing the grain boundary diffusion process (GBD) were recycled by the so-called functional or short-loop recycling approach, based on hydrogen decrepitation (HD). Microstructural and magnetic differences between the original and the recycled materials were analyzed. The functional recycling of GBD magnets leads to the dissolution of the core (heavy rare earth lean) - shell (heavy rare earth rich) structure through the different heat treatment steps which include hydrogen decrepitation, sintering, and annealing. The recycled magnets show similar rectangular demagnetization curves with squareness of 96 %, and only a slightly decreased remanence of 5 % to 1.31 T, but a larger decrease in coercivity of 21 % to 1703 kA/m. A new GBD step using 1.5 wt.% Tb with a pure Tb-foil as diffusion source leads again to the formation of a core-shell structure with 0.5 μm thick Tb-shells which is similar to the microstructure of the original magnets prior to recycling. The coercivity of the recycled magnets is increased by 35 % from 1315 kA/m to 1780 kA/m at 50 °C and shows similar magnetic values as the original industrial magnets at 150 °C and 200 °C, respectively. The temperature coefficients for the remanence, α, and for the coercivity, β, can also be fully restored and even exceed the original values which leads to an improved temperature stability of the recycled magnets compared to the original magnets.

1. Introduction

Rare earth permanent magnets, especially Nd-Fe-B-type magnets, play a vital role in many key technologies like robotics, renewable energy, and electromobility [1,2]. The global demand for Nd-Fe-B magnets is projected to drastically increase from 20,847 kt in 2022 to 121,042 kt in 2035, due to the growth of electric car stock and the use of these materials in the drive train of electric vehicles [3]. For such applications that expose the magnets to elevated temperatures (such as in electric motors), a high coercivity is necessary to compensate temperature-dependent losses. A common method to achieve this goal is the use of heavy rare earth (HRE) elements like Dy or Tb, due to the higher magnetocrystalline anisotropy of $Dy_2Fe_{14}B$ or $Tb_2Fe_{14}B$ compared with $Nd_2Fe_{14}B$ [4]. However, these HRE elements are very critical substances of high strategic relevance in multiple respects,

resulting in high prices, price volatility and substantial supply risks. The market is dominated by a few suppliers using deposits mostly in Southern China and the mining and refining of RE elements is associated with very high environmental burdens when applying current practices. As an example, the production of one ton REE oxide yields up to 1.4 tons radioactive waste (depending on the deposit), 1000 tons of wastewater and 2000 tons of waste material [5,6]. The recycling of RE magnets is therefore an essential option to increase the sustainability and decrease the dependencies in the supply chain of electric vehicles and multiple further products that are key for renewable energy supply and the sustainable electrification of industry and society [7–10]. Depending on chemical composition, impurity content, dispersion, system integration and physical state of the End-of-Life (EoL) magnets, different recycling techniques can be used [11–14]. The direct or functional recycling approach, using hydrogen, can lead to the production of recycled

* Corresponding author.
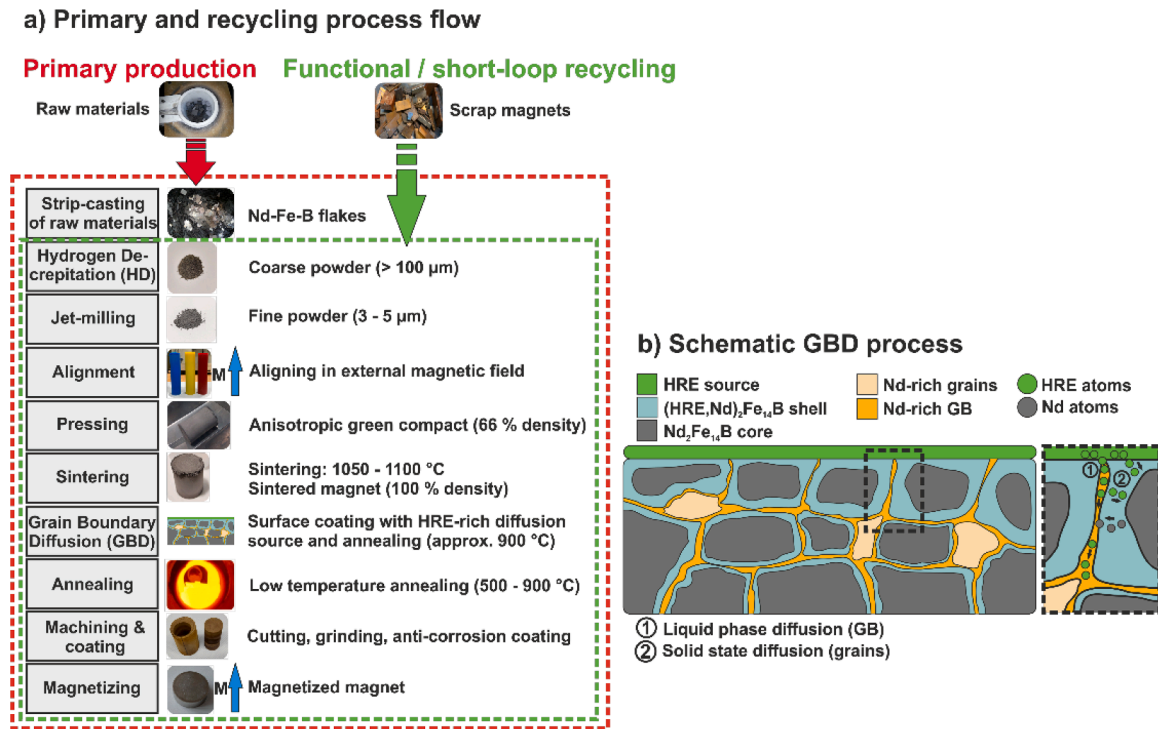*E-mail address:* mario.schoenfeldt@iwks.fraunhofer.de (M. Schönfeldt).

Fig. 1. Schematic illustration of the primary and functional recycling process flows for the production of sintered Nd-Fe-B magnets (a) and schematic illustration of the GBD process and resulting microstructure (b).

magnets without the need of high amounts of energy or chemicals and can be readily implemented into the regular primary production process, since it uses the same manufacturing infrastructure and processing techniques [15,16].

In view of this complex scenario, the use of HRE counts as the primary disadvantage of permanent magnet (PM) type traction motors [17]. To reduce the required content of HRE elements in high coercive magnets, different techniques were developed over the last years: (1) grain size refinement; (2) modification of grain boundary phase e.g. $R_6(Fe,M)_{14}$; and (3) the Grain Boundary Diffusion Process (GBD) [18]. The GBD was first proposed by Park *et al.* in 2000 [19] and recently successfully implemented into industrial magnet production. This process results in a core-shell type microstructure consisting of $Nd_2Fe_{14}B$ grains with a HRE-rich shell and a HRE-lean core. The magnet surface is coated with a HRE-rich diffusion source and during a specific heat treatment, the HRE elements diffuse from the surface of the magnet along the liquid grain boundary phase (GB) into the bulk and grain interior and lead to the formation of a $(Nd,HRE)_2Fe_{14}B$ shell on the outer region of the $Nd_2Fe_{14}B$ grains [4]. This is a pertinent approach because the HREs are only needed at these outer regions of the $Nd_2Fe_{14}B$ matrix grains because the formation of reversed domains and demagnetization processes, which would reduce the coercivity and hence the hard magnet's performance, starts typically at the weakest microstructural spots in nucleation-type permanent magnets (e.g., $Nd_2Fe_{14}B$ or $SmCo_5$), namely, at the grain boundaries, edges of grains and other lattice defects. The term 'nucleation-type permanent magnet' refers to a coercivity mechanism which is easily recognized by a high initial susceptibility $\chi = dM/dH$ upon magnetization coming from the thermally demagnetized state [20]. As an example the $(Nd,HRE)_2Fe_{14}B$ shell leads to a magnetic hardening effect which suppresses the formation of reversed domains and therefore results in an improved coercivity value. It was shown that next to the grain boundaries the crystalline structure of $Nd_2Fe_{14}B$ matrix phase can be distorted reducing the magnetocrystalline anisotropy in such regions, which in turn promotes the nucleation of reversed domains [21]. At the same time, the substituted Nd atoms diffuse from the $(Nd,HRE)_2Fe_{14}B$ grain into the grain boundary phase, which leads to a better magnetic decoupling of the individual grains and therefore to higher coercivity values [22]. Compared to traditional alloying methods with HREs, the advantages of the GBD method consist in only a minimal loss in remanence caused by an antiferromagnetic coupling of HRE with Fe and a reduction of the necessary HRE content in the whole magnet. Fig. 1 shows a schematic illustration and comparison of the primary production and functional recycling process steps and illustrates the typical core-shell microstructure after the GBD process.

After the discovery of the GBD by Park *et al.* [19], many efforts were undertaken to improve and optimize the GBD process in terms of HRE content and microstructure. Different diffusion sources and coating techniques were developed and analyzed in detail: examples are dip-coating or electrophoretic deposition of HRE-fluorides or oxides [23–25], HRE-rich alloys [26,27] and pure HRE in form of platelets, foils or through vapor deposition or sputtering [28–32]. A comprehensive overview of the different methods and results achieved has been given by Liu et al. [33]. Common to all methods is the diffusion annealing after coating at approximately 900 °C, followed by a low-temperature annealing at about 500 °C. The diffusion of HRE inside the magnet is divided into a faster liquid phase diffusion along the grain boundaries and a slower solid state diffusion inside the grains to form the HRE-rich shells [34]:

$$c(x,t) = \varphi c_{GP}(x,t) + (1-\varphi)c_{GBP}(x,t) \tag{1}$$

where x is the diffusion depth, t is the diffusion time, $C_{GP}(x, t)$ is the distribution of the HREs in the grains, $C_{GBP}(x, t)$ is the distribution of the HREs in the grain boundary phase, φ is the volume fraction of the interface-free grain phase and $1-\varphi$ is the volume fraction of the grain boundary phase. The RE concentration profile along the grain boundaries to the center of the magnet can be described as follows [32]:

$$c(x,t) = c_{surf} - (c_{surf} - c_{bulk}) \times erf\left(\frac{x}{\sqrt{4Dt}}\right) \tag{2}$$

where D is the diffusion constant and c_{surf} and c_{bulk} are the surface and

bulk concentrations, respectively.

Recent work to that end is concerned with the formation of a so-called double core-shell structure, consisting of a Dy and Tb shell instead of only one HRE-rich shell through the combination of the so-called double alloy method in conjunction with the application of a GBD process [35–37]. To prevent the use of critical and expensive HRE, the research focus lies now on the implementation of a GBD process with HRE-free diffusion sources like low-melting eutectics e.g., $Nd_{70}Cu_{30}$, $Nd_{90}Al_{10}$, $Nd_{80}Ga_{15}Cu_5$, or $La_{71}Cu_{29}$ [38] or non-RE compounds or alloys like MgO, ZnO or AlCu [39]. The GBD was also implemented successfully on waste magnets to increase coercivity [40,41] and on recycled traditional alloyed magnets [42]. However, even with an optimized core-shell microstructure and a reduced HRE content of approx. 2 wt.% compared to traditional alloying [43], RE-based permanent magnets are still considered as highly critical, not because REEs are rare but because in a multi-factor criticality assessment e.g. the monopolistic raw materials supply situation and current extraction and separation methods continue to be problematic [44].

In this work, commercially available GBD magnets were recycled using the functional recycling approach via hydrogen decrepitation (HD) and material embrittlement at 3 bar partial pressure of H_2 and room temperature. The HD process utilizes the pronounced but differential lattice expansion upon interstitial hydrogen absorption into both the $Nd_2Fe_{14}B$ matrix and rare earth rich grain boundary phases [45]. Investigations on the changes of the GBD microstructure (core-shell) and magnetic properties through the recycling process were conducted in detail, addressing relevant questions on how the powder metallurgical recycling process can influence the impurity uptake (oxygen, nitrogen and carbon), core-shell microstructure development and magnetic properties.

2. Experimental procedure

GBD magnets from industrial magnet production with the dimensions of 19.7×5.2×5.3 mm and the nominal composition of $Nd_{23.0}Pr_{6.15}Tb_{1.76}Dy_{0.24}Fe_{bal}B_{0.93}Co_{0.89}Ga_{0.21}Al_{0.13}Cu_{0.08}$ (wt. %), hereinafter referred to as GBD scrap magnets, were recycled with the so-called functional or short-loop recycling approach under the use of hydrogen decrepitation (HD). Over 100 magnets (0.5 kg in total) were decrepitated to a coarse powder (D_{50}: 234 μm) under 3 bar hydrogen for 4 h, followed by a dehydrogenation step at 500 °C for 3 h under vacuum and cooling to room temperature under argon atmosphere. The coarse powder was then milled to a particle size D_{50} of 5.4 μm with a target jet-mill using a Si_3N_4 target (MJQ Lab, Hosokawa Alpine AG) under nitrogen atmosphere. The particle size distributions of the coarse HD and milled powder can be seen in the supplementary material of this publication. Then, the powder was magnetically aligned and pressed in a transversal field press under argon atmosphere with an external magnetic field of 2.5 T, followed by sintering in a tube furnace under vacuum (10^{-6} mbar) in the range between 1050 °C and 1100 °C for a duration between 2 and 6 h, to obtain fully dense anisotropic sintered magnets. After the sintering process, multiple low temperature annealing steps between 500 °C and 900 °C for 1 h under vacuum were conducted to optimize the material's magnetic properties. The best magnetic properties could be obtained when applying a temperature-time profile of 1100 °C for 4 h (sintering) followed by 700 °C for 1 h and 500 °C for 1 h (annealing). Some of the recycled magnets were finally used again for grain boundary diffusion experiments with 1.5 wt.% pure Tb-foil at 900 °C for 9 h with subsequent low-temperature annealing. To analyze the influence of the different heat treatments during the recycling process on the magnetic and structural properties, some of the GBD scrap magnets were annealed between 500 °C and 1100 °C under vacuum (10^{-6} mbar).

The magnetic properties were measured using a hysteresis graph (Permagraph C, Magnet-Physik Dr. Steingroever GmbH) and a HyMPulse – Hysteresis measurement system (Metis Instruments & Equipment N.V.) in external fields up to 7 T. The concentration of impurities like oxygen, nitrogen and carbon were measured with hot gas extraction (LECO ONH-836-MC and CS-744-MHPC analyzer) and the chemical composition was determined by inductively coupled plasma optical emission spectrometry (ICP-OES) analysis (OPTIMA 8300 DV, PerkinElmer LAS Germany GmbH). The mass density was measured with an analytical balance according to Archimedes principle and analysis of the particle size distribution was conducted by laser diffraction (Mastersizer 3000, Malvern Instruments GmbH). Microstructural investigation was performed with a Carl Zeiss Cross Beam 540 and Carl Zeiss MERLIN microscope through high-resolution scanning-electron microscopy (SEM) in conjunction with the back-scattered electron (BSE) imaging technique and energy dispersive X-ray spectroscopy (EDS). For SEM analysis bulk magnets were prepared using a Leica EM TIC 3X Ion Beam Milling (IBM) System and powder samples were prepared using a Focused Ion Beam (FIB) technique. To ensure the comparability of these measurements on the GBD magnets, where the microstructure changes from the edge to the core of the materials, all EDS mappings or line scans were conducted at the same distance (200 - 400 μm) from the surface of the magnets. Electron backscatter diffraction (EBSD) for crystallographic texture and phase probing was performed in conjunction with chemical indexing (Chi scan assisted by energy dispersive X-ray spectroscopy) using a Zeiss Merlin microscope operated at an accelerating voltage of 15 kV. The step size of the EBSD measurement was 80 nm. The acquired EBSD and EDS data were analyzed using the OIM AnalysisTM V8.6 software package to extract information on the grain size and crystallographic texture of the microstructure of the investigated materials. The grain size analysis encompassed 8545 and 9606 grains for the scrap and recycled magnet, respectively. The analysis thresholds were from 1 μm to 20 μm grain diameter and binned with 25 bins. For quantitative texture analysis, orientation distribution functions (ODF) have been calculated through a series expansion method using symmetrized spherical harmonic library functions. The series expansion was performed for the case of orthotropic sample symmetry with rank 22, 1° orientational step width and Gaussian smoothing of 5°. For more convenient interpretation purposes the data then was plotted in sections through the symmetry-reduced Euler space. A Ga-FIB (Helios 5 CX) was used to prepare the needle-shaped atom probe tomography (APT) samples using a standard sample preparation protocol described in [46]. APT experiments were performed using a Cameca LEAP 5000 XR (reflectron) atom probe. A reflectron APT instrument uses a magnetically enhanced ion flight path for obtaining higher mass-to-charge resolution, to better distinguish the different RE elements in the spectra. The APT measurements were performed in laser pulsing mode with a laser energy of 50 pJ with a repetition rate of 125 kHz at a base sample temperature of 50 K with a detection rate of 1.0 ion per 100 pulses on average. Data reconstruction was performed using Cameca's Integrated Visualization and Analysis Software (IVAS) in AP Suite 6.3. For determination of crystalline phases, a PANalytical Empyrean X-ray diffractometer with Co $K\alpha_{1,2}$ radiation was used. The magnetic domain structures were observed in polar contrast with a Magneto-optical Kerr microscope (MOKE) (Evico magnetics GmbH). The magnetic domains were probed along the easy magnetization axis in samples which were thermally demagnetized state and after being magnetized in an external magnetic field of 7 T using a Metis Pulse Field Magnetometer. For the calculation of the temperature coefficients and the evaluation of the temperature stability of scrap and recycled magnets, all samples were characterized at elevated temperatures up to 200 °C in 50 °C steps. The temperature coefficient for the change of remanence as a function of temperature change, α, and the one for coercivity change, β, were calculated according to the following equations

$$\alpha = \frac{1}{B_r} \times \frac{dB_r}{dT} \times 100 \ (\%/°C) \tag{3}$$

$$\beta = \frac{1}{H_{cJ}} \times \frac{dH_{cJ}}{dT} \times 100 \ (\%/°C) \tag{4}$$

Table 1

Chemical composition of GBD scrap magnets and recycled magnets before and after recycling and grain boundary diffusion process.

	Elemental composition (wt.%)									
Sample	Nd	Pr	Tb	Dy	Fe	B	Co	Ga	Al	Cu
GBD scrap magnet	23.0	6.15	1.76	0.24	bal	0.93	0.89	0.21	0.13	0.08
Recycled magnet	23.0	6.21	1.73	0.25	bal	0.95	0.92	0.22	0.13	0.09
Recycled magnet after Tb-GBD	22.9	6.18	2.20	0.25	bal	0.95	0.91	0.20	0.13	0.08

Table 2

Impurity content of magnets before and after functional recycling.

	Impurity content (wt.%)		
Sample	O	N	C
GBD scrap magnet	0.172	0.089	0.040
Recycled magnet	0.296	0.124	0.050

where B_r is the remanence and H_{cJ} the coercivity of the magnet, measured at two temperatures, respectively.

3. Results and discussion

3.1. Chemical composition and impurities intruding through functional recycling by using hydrogen

Table 1 shows the chemical compositions of the GBD scrap magnets and the recycled magnets before and after the recycling process and the applied grain boundary diffusion process. The composition remains nearly constant through the functional recycling process, indicating no significant element-specific losses during recycling. Small deviations within some elements are in the accuracy of the measuring method. All measured compositions fall within the typical range of sintered magnets sold in the market [47]. The GBD scrap magnets show a total rare earth content (TRE) of 31.2 wt.%. The applied GBD after recycling, performed with 1.5 wt.% (referred to the magnet mass) Tb-foil on the recycled magnet, leads to a Tb-content increase of 0.5 wt.%.

The impurity content (oxygen, nitrogen and carbon) of the primary GBD scrap magnets and recycled magnets is shown in Table 2. It increases slightly during the recycling process. The GBD scrap magnets show an oxygen content of 0.172 wt.%, increasing to 0.296 wt.% in case

of recycled magnets. Also, the amount of nitrogen and carbon increases from 0.089 wt.% to 0.124 wt.% and from 0.040 wt.% to 0.050 wt.%, respectively. Even when using very pure argon atmosphere or vacuum (5.0 Argon with purity $\geq$ 99,999 % and 10^{-6} mbar in the present case) throughout the whole recycling process, an impurity pick-up is expected and observed. To overcome this issue, either additional RE elements can be added to the recycled material or the oxidized particles can be separated from non-oxidized material [16,48]. However, despite the uptake of oxygen and nitrogen, the impurity content of the recycled magnet is still comparable to commercially available sintered magnets [47].

3.2. Magnetic properties of recycled and annealed GBD scrap magnets

When probing the GBD scrap magnets as starting material we observe a rectangular demagnetization curve with a squareness (*SQ*) of 96 %, a remanence (*Br*) of 1.38 T, a coercivity (*HcJ*) of 2143 kA/m, and an energy product ((*BH*)$_{max}$) of 364 kJ/m^3. The SQ metric can be calculated from the knee field strength $H_{k,90}$ (the field strength, at the point at which J is reduced by 10 %) and the coercivity H_{cJ} according to

$$SQ = H_{k,90} / H_{cJ} \qquad (5)$$

The recycled magnet shows the same *SQ* ratio of 96 %, with a slightly decreased remanence of 1.31 T (ΔB_r = -5 %) and (*BH*)$_{max}$ of 328 kJ/m^3 which can be related to a different pressing method and degree of alignment [16] and to the increase of the overall impurity content, which can also affect the coercivity and remanence of the recycled magnets [49]. As for H_{cJ}, a larger decrease to 1703 kA/m (decrease of 21 %) can be observed (Fig. 2a). This large drop in coercivity is mainly caused by microstructural changes as will be discussed in Section 3.3. The GBD scrap magnet shows a mass density of 7.58 g/cm^3, while the recycled magnet has a slight decreased mass density of 7.53 g/cm^3
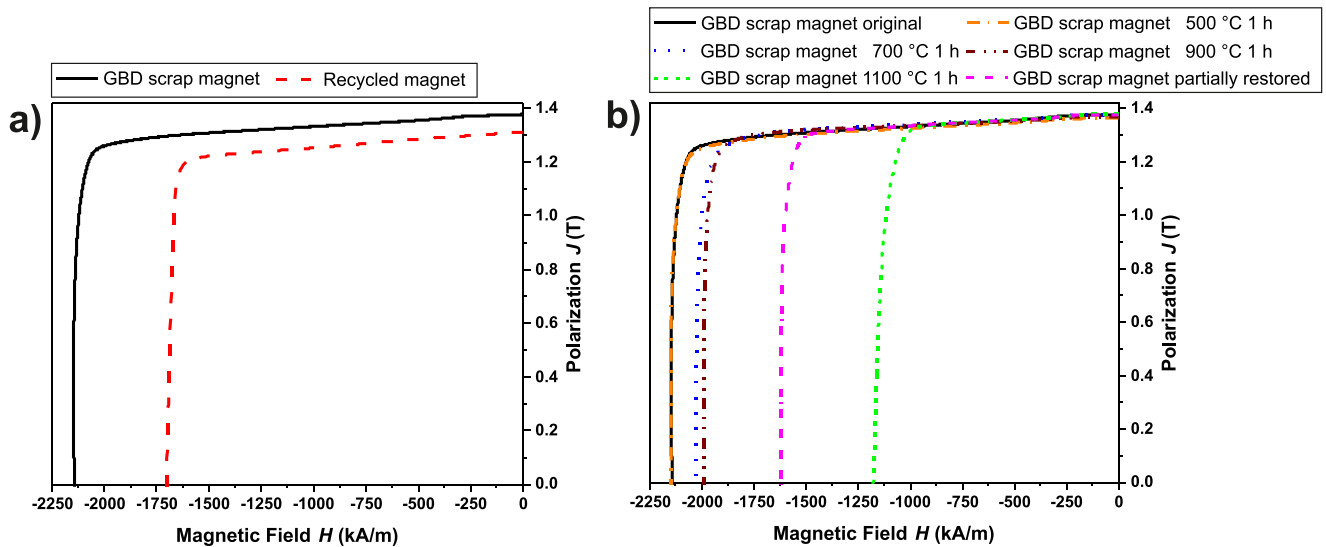

Fig. 2. Demagnetization curves of the GBD scrap magnet and of the recycled magnet (a) and demagnetization curves of GBD scrap magnets which were annealed at different temperatures (b). The magnet with partially restored coercivity was additionally annealed at low temperatures, namely, 1100 °C 1 h + 700 °C 1 h + 500 °C 1 h.
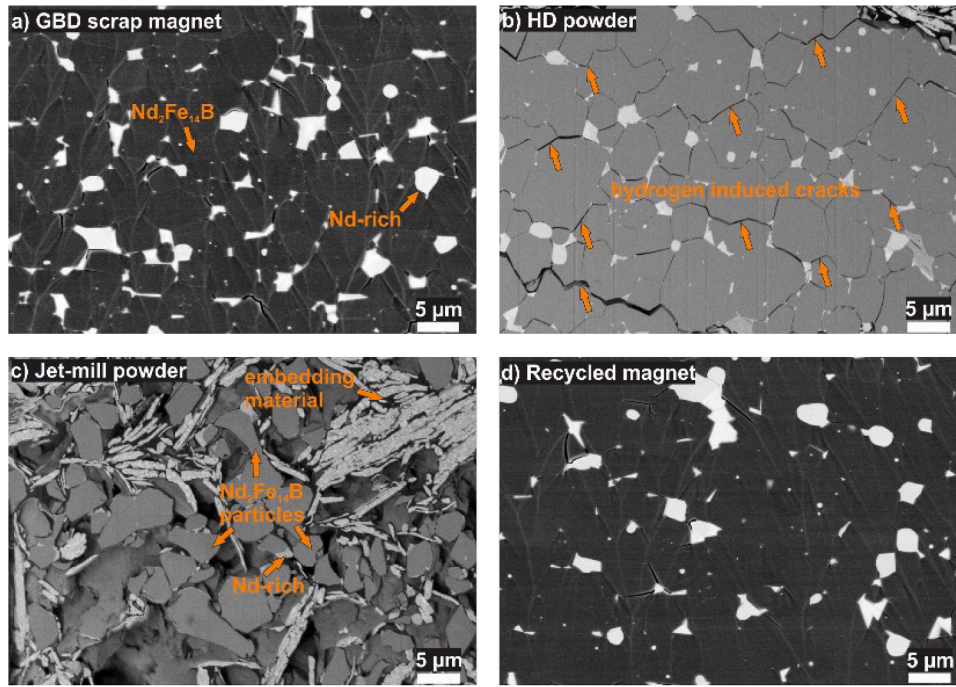
Fig. 3. SEM BSE overview images of GBD scrap magnet (a), HD powder (b), jet-mill powder (c), and recycled magnet (d). In the case of the HD powder, the cracks between the individual $Nd_2Fe_{14}B$ matrix grains, caused by hydrogen decrepitation and volume expansion, are clear visible. Vertical lines are preparation artefacts from IBM or FIB procedures.
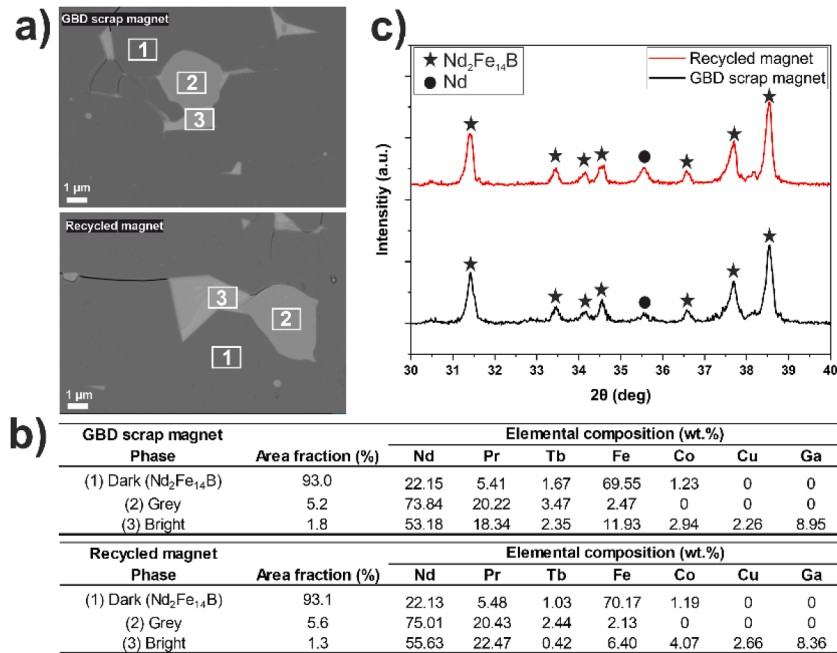

GBD scrap magnet

Phase	Area fraction (%)	Elemental composition (wt.%)						
		Nd	Pr	Tb	Fe	Co	Cu	Ga
(1) Dark ($Nd_2Fe_{14}B$)	93.0	22.15	5.41	1.67	69.55	1.23	0	0
(2) Grey	5.2	73.84	20.22	3.47	2.47	0	0	0
(3) Bright	1.8	53.18	18.34	2.35	11.93	2.94	2.26	8.95

Recycled magnet

Phase	Area fraction (%)	Elemental composition (wt.%)						
		Nd	Pr	Tb	Fe	Co	Cu	Ga
(1) Dark ($Nd_2Fe_{14}B$)	93.1	22.13	5.48	1.03	70.17	1.19	0	0
(2) Grey	5.6	75.01	20.43	2.44	2.13	0	0	0
(3) Bright	1.3	55.63	22.47	0.42	6.40	4.07	2.66	8.36

Fig. 4. SEM images with marked EDS measurement areas (a), composition of different phases (b) and XRD patterns (c) of the GBD scrap magnet and the recycled magnet. The recycled magnet was sintered at 1100 °C for 4 h and annealed at 700 °C for 1 h and 500 °C for 1 h.

which can be related to the impurity uptake. For further investigation of the coercivity decrease, the GBD scrap magnets were annealed under vacuum (10^{-6} mbar) at different temperatures and times (Fig. 2b). While the remanence of the GBD scrap magnets is not influenced by the annealing, the coercivity shows a reduction with increasing annealing temperature from 500 °C to 1100 °C. After a relative unaffected coercivity of 2147 kA/m (500 °C), which is close to the value observed in the original GBD scrap magnet (2143 kA/m), H_{cJ} decreases to 2030 kA/m

(700 °C), 1992 kA/m (900 °C), and 1177 kA/m (1100 °C). The annealing temperature used for sintering (1100 °C) shows the largest influence on H_{cJ}, with 45 % reduction relative to the starting material, but can be partially restored to 1617 kA/m with a subsequent low-temperature annealing at 700 °C and 500 °C after the annealing at 1100 °C. This large coercivity decrease through heating at a specific transition temperature and the partial recovery after an additional low-temperature annealing of the GBD magnets, was also observed by Sepehri-Amin *et*
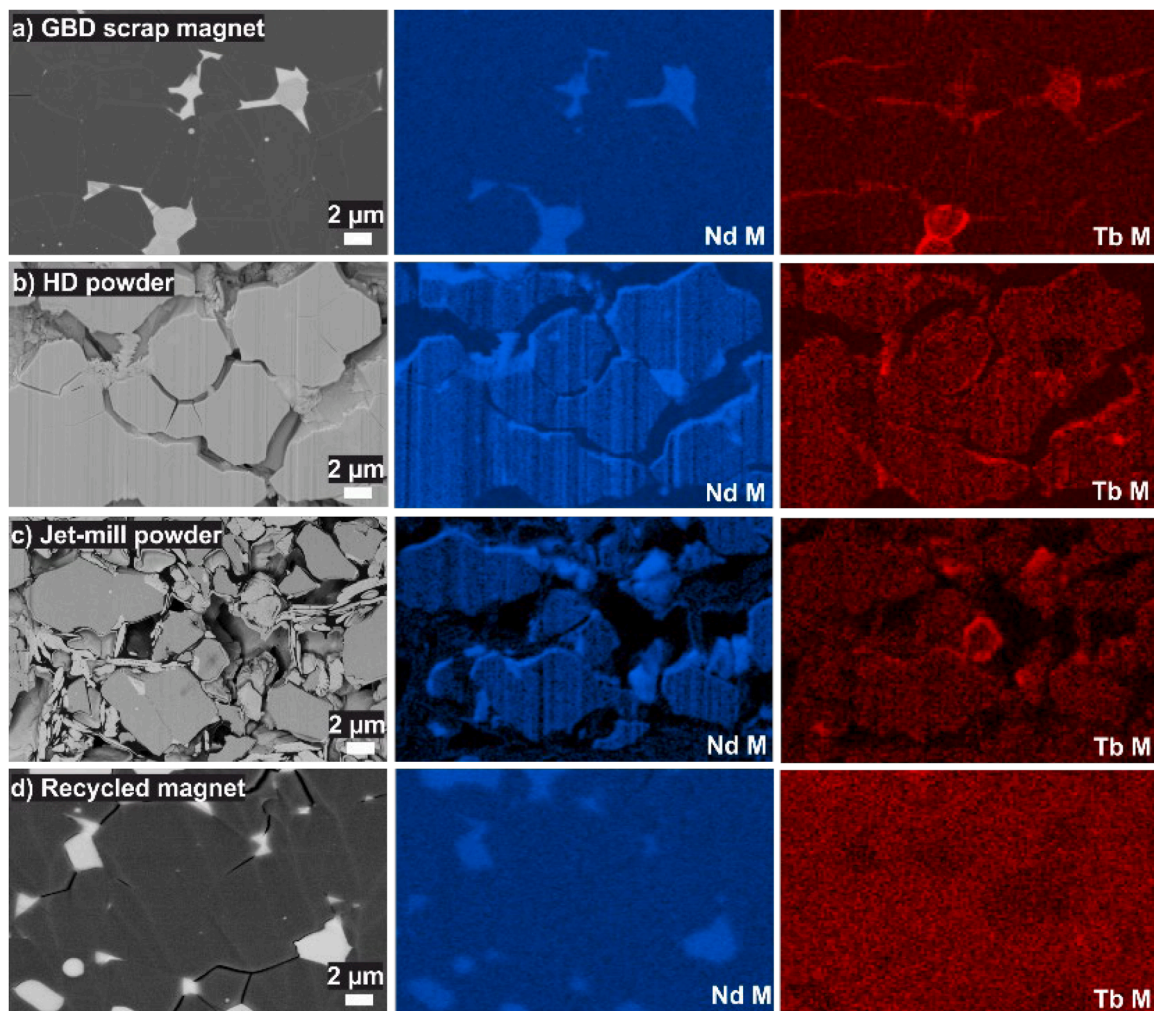
Fig. 5. SEM-BSE images with EDS mappings of GBD scrap magnet (a), HD powder (b), jet-mill powder (c) and recycled magnet (d). While at the GBD scrap magnet several Tb-core-shells can be observed, the other samples show less clear core-shell formation through the functional recycling process, but Tb enrichments at the outer regions of the grains.

al. [50]. As will be shown and discussed in Section 3.3, the microstructure of a sintered Nd-Fe-B magnet consists of tetragonal $Nd_2Fe_{14}B$ ferromagnetic matrix grains, with sizes in the micrometer range, surrounded by a Nd-rich GB phase and Nd-rich grains at the triple junctions. The Nd-rich GB phase leads to a magnetic decoupling of the individual grains, i.e. it reduces the exchange interactions leading to an improvement of coercivity [50]. Here, a homogenous and continuous distribution of the GB phase within the whole magnet is important to gain the highest coercivity values. A non-optimized post-sinter annealing temperature can result in an inhomogeneous GB phase distribution with insufficient magnetic decoupling of the grains and increased local stray fields around grain boundary cracks, which is responsible for a reduction in the coercivity value [51–55]. It was reported by Sepehri-Amin et al. [50], that the reason for the large coercivity decrease after a heat treatment was an inhomogeneous distribution of the GB phase layer, which can be partially restored again through the application of a low temperature annealing treatment at an optimum annealing temperature through the formation of a continuous GB phase layer. In the same study, a large decrease of 63 % was observed after annealing at 900 °C, instead of a reduction of 7 % at 900 °C and 45 % at 1100 °C in our study. The permanent or remaining loss of coercivity even after partial recovery assumes a wide loss range, with values between 39 % [50] and 25 % (this study), respectively. Reasons for these differences can be associated to the different diffusion coefficients of Dy and Tb ($8.45 * 10^{-7}$ cm^2/s and $1.23 * 10^{-6}$ cm^2/s, according to [32] respectively) and/or

differences in the overall chemical composition and grain size distribution of the magnets under investigation. Woodcock et al. [47] analyzed the recovery of coercivity of commercially available Dy-free and Dy-containing magnets (traditionally alloyed magnets, not GBD magnets). It was found that a coercivity reduction of 30 % after heating at 1050 °C is reversible and fully repeatable. The authors also confirmed, that the decrease in coercivity is due to the formation of an inhomogeneous GB phase and can be recovered through the reformation of a homogenous GB phase distribution. Therefore, the partial recovery of the coercivity H_{cJ} after a low temperature annealing observed in this study can be explained by restoring of a homogenous GB phase distribution. The reason for the observed remaining permanent loss of H_{cJ} in this study and the study from Sepehri-Amin et al. [50] could be in the GBD microstructure with $(Nd,HRE)_2Fe_{14}B$ shells which was not observed in the study published by Woodcock et al. [47]. According to Fidler [56], the grain size and its distribution, misorientation, and different phases can influence on the gained coercivity of magnets, whereby long-range dipolar interactions reduce the coercive field of ideally oriented particles by about 20 % and short-range exchange coupling between misaligned grains leads to a reduction of 30 % – 40 % of the ideal nucleation field. A permanent alteration in the microstructure could be identified as the reason why H_{cJ} was unable to fully recover following the low-temperature annealing at 700 °C and 500 °C (see Section 3.3).
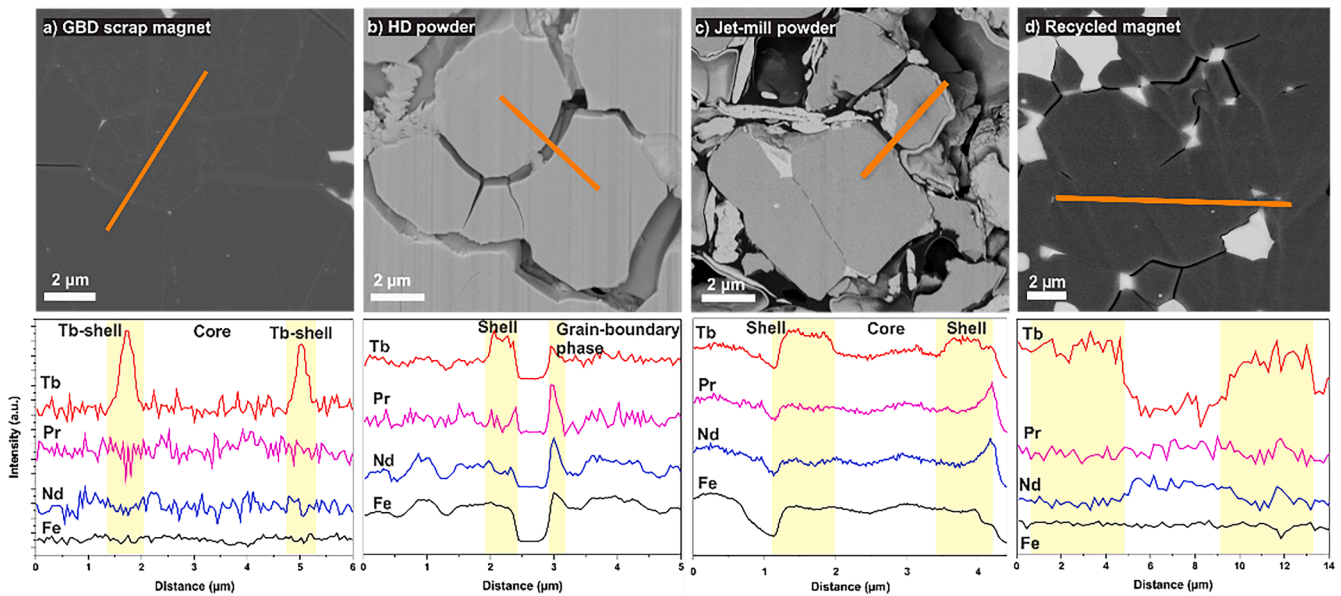
Fig. 6. SEM BSE images and EDS line scans of GBD scrap magnet (a), HD powder (b), jet-mill powder (c) and recycled magnet (d). While at the GBD scrap magnet a narrow Tb-core-shell structure with 0.5 μm can be observed, the other samples show less clear core-shell formation but broader Tb enrichments at the outer regions of the grains. For comparability, the intensities of the EDS line scans are normalized.

3.3. Microstructural characterization

The initial microstructure of the GBD scrap magnet in Fig. 3a consists of typical $Nd_2Fe_{14}B$ matrix grains (dark contrast) which are surrounded by rare earth rich grain boundary phases and triple junctions (bright contrast). At the outer regions of the grains, heavy rare earth Tb-rich shells are visible (Figs. 5a and 6a). During hydrogen decrepitation, intergranular cracks along the grain boundaries are formed as shown in Fig. 3b, leading to the embrittlement and formation of a coarse powder which can then be jet-milled to a finer particle size (Fig. 3c). The recycled magnet (Fig. 3d) shows a homogenous microstructure of $Nd_2Fe_{14}B$ grains and RE-rich phases and without cracks or pores. It is notable that no core-shell structures are visible in the BSE images of powder samples and the recycled magnet.

The RE-rich phase shows two different types of contrast, indicating that there seem to be two different types of RE-rich phases present. To analyze the chemical composition of these phases an EDS area scan was performed on the dark appearing $Nd_2Fe_{14}B$ phase and also on both RE rich phases observed in the GBD scrap magnet and also in the recycled magnet materials (Fig. 4a). The chemical composition of all phases is presented in Fig. 4b. The $Nd_2Fe_{14}B$ matrix phase shows a total rare earth (TRE) content of 29.4 wt.% and 1.2 wt.% Co. While Co is present in the $Nd_2Fe_{14}B$ phase, Cu and Ga are only detectable in one of the two types of RE rich phases. The bright phase consists of 73.9 wt.% RE elements, 11.9 wt.% Fe, and low amounts of Co, Cu and Ga. Compared to that, the grey RE phase shows a TRE content of 97.5 wt.%, 2.5 wt.% Fe and no Co, Cu and Ga. The whole microstructure consists of 93.0 % $Nd_2Fe_{14}B$, 5.2 % grey RE, and 1.8 % bright RE phase. The area fraction was determined using the SEM software at three different positions of the magnet cross-section within an area of 110×80 μm to analyze a statistically representative number of grains. Compared to the GBD scrap magnet, the recycled magnet shows 0.1 area % less RE-rich phase. The overall composition of the three phases is similar to the primary magnet, but the amount of RE elements differ, which could be related to the heat treatment through functional recycling of the magnets. The TRE of the main phase and of the grey appearing RE phase is similar as in the primary magnets with 28.6 wt.% and 97.9 wt.%, respectively. The bright appearing phase with 78.5 wt.% TRE shows an increase of 4.6 wt.% compared to the GBD scrap magnet. A reason for this change in elemental distribution could be the sintering and annealing processes

applied in the recycling procedure. The XRD patterns (Fig. 4c) of both magnets shows very similar patterns, with most diffraction peaks belonging to the $Nd_2Fe_{14}B$ phase, except the reflex at 35.59° which represents metallic Nd. The integrated intensity of this reflex is higher for the recycled magnet than for the primary one, indicating a higher amount of secondary phase. This could be related to the higher amount of RE-rich bright phase in the recycled magnet.

As mentioned above, the Tb-rich shell regions are not discernable in the SEM-BSE images at the outer regions of the $Nd_2Fe_{14}B$ grains in the material obtained through the functional recycling process. The EDS compositional mappings in Fig. 5 show an enrichment of Tb at the outer regions of the grains in the case of primary magnet. In addition to Tb-lean particles, Tb-accumulations can also be seen on individual particles of HD powder and jet-mill powder. For the recycled magnet no clear shells can be found, but there is also a depletion of Tb in the center of the $Nd_2Fe_{14}B$ grains, which indicates a smearing or broadening of the Tb shells.

This smearing or broadening of the Tb shells can be seen clearer in the EDS line scans of Fig. 6. The marked areas within the line scans reveal regions with Tb enrichment. The $Nd_2Fe_{14}B$ grains of the GBD scrap magnet show a narrow Tb-shell of approximately 0.5 μm thickness. At the same position, with the increase of the Tb content, a concurrent decrease in Pr and Nd can be observed, related to the partial substitution of Pr and Nd with Tb through the formation of $(Nd,Pr,Tb)_2Fe_{14}B$ shells. Also, in both types of powder samples (HD and jet-mill), a Tb enrichment at the edges of grains with thicknesses of 0.5 – 0.8 μm can be observed. However, due to the large number of cracks and other defects between the individual grains, an accurate measurement is difficult. Compared to these samples, the recycled magnet shows larger Tb enrichment zones with up to 4 μm thickness. The reason for this broadening of the Tb-rich shells could be the heat treatment processes during functional recycling. The material had been heated at 500 °C for 3 h in the HD process and 1100 °C for 4 h followed by 700 °C for 1 h and 500 °C for 1 h for sintering and annealing. In the literature, different values for the Tb grain boundary diffusion coefficient D_{Tb} in Nd-Fe-B magnets can be found. Huang et al. [57] calculated a coefficient D_{Tb} of $7.02 \pm 0.12 *10^{-8}$ cm^2/s at 850 °C, and Löwe et al. [32] determined a higher value of $1.23 \pm 0.84*10^{-6}$ at 900 °C. Taking these values as upper and lower bounds, respectively, a diffusion depth in the range of several hundred μm during the whole heat treatment process of 9 h is
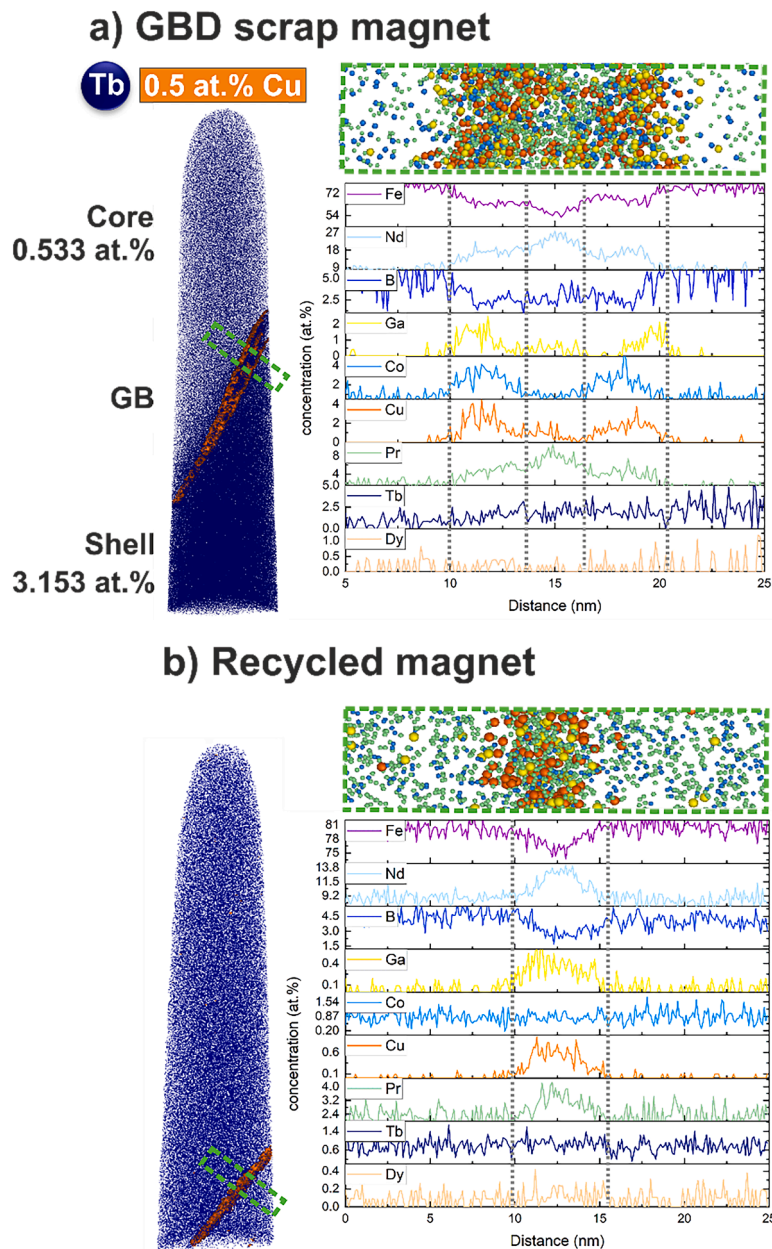
Fig. 7. APT investigation of a) GBD scrap magnet and b) recycled magnet reveals beside a more homogenous distribution of Tb and disappearance of the core-shell microstructure also changes in the grain boundary elemental distribution. The chemical concentration plots presented next to the APT reconstructions are obtained from the area marked with green dashed rectangles that cross over a grain boundary (GB). The enlarged region of interest with the reconstruction is presented above the diagram. The grain boundary in the reconstruction is visualized through orange coloration that is set by the 0.5 at.% Cu enrichment. The color of the atoms corresponds to the color of the line scans.

possible. Note that these diffusion coefficients contain liquid phase diffusion (see Eqs. (1) and (2)) which is several orders of magnitude larger than solid state diffusion and associated solid state movement of Tb atoms from the shell to the center of the grain. Therefore, a change in the lower μm range within the shell during the recycling process is possible.

Atom probe tomography (APT) analysis confirms the core-shell structure for the GBD scrap magnets, a microstructure feature which was not observed for the recycled magnets (see Fig. 7). Before recycling, a Tb-lean area with 0.5 at.% Tb (core) is separated from a Tb-rich area with 3.2 at.% Tb (shell) by the grain boundary phase (GB). After recycling, a homogenous Tb distribution with approx. 0.6 at.% is measured. Besides a more homogenous Tb distribution, also differences in the elemental distribution of the grain boundary (GB) phase can be seen in

the recycled magnet. The GBD scrap magnet shows a double layer or double peak of the elements Ga, Co and Cu with enrichment at the outer region of the GB phase and near the grains. For the recycled magnet, these elements are more homogenously distributed along the whole GB phase. This change can also lead to differences in the coercivity of both magnets, such as through increased decoupling of the grains for the GBD scrap magnet due to the virtual increase of the decoupling distance by the multilayered structure of the GB phase.

The comparison of the EBSD results indicate that the recycled magnet exhibits a slight refinement of the average grain size: the recycled magnet has on average a higher number of smaller-sized grains in the range of 1 - 2.5 μm, compared to the GBD scrap magnet. In contrast, the GBD scrap magnet presents a higher number of smaller-sized grains in the range of 2.5 - 5 μm. These differences can be clearly seen from the
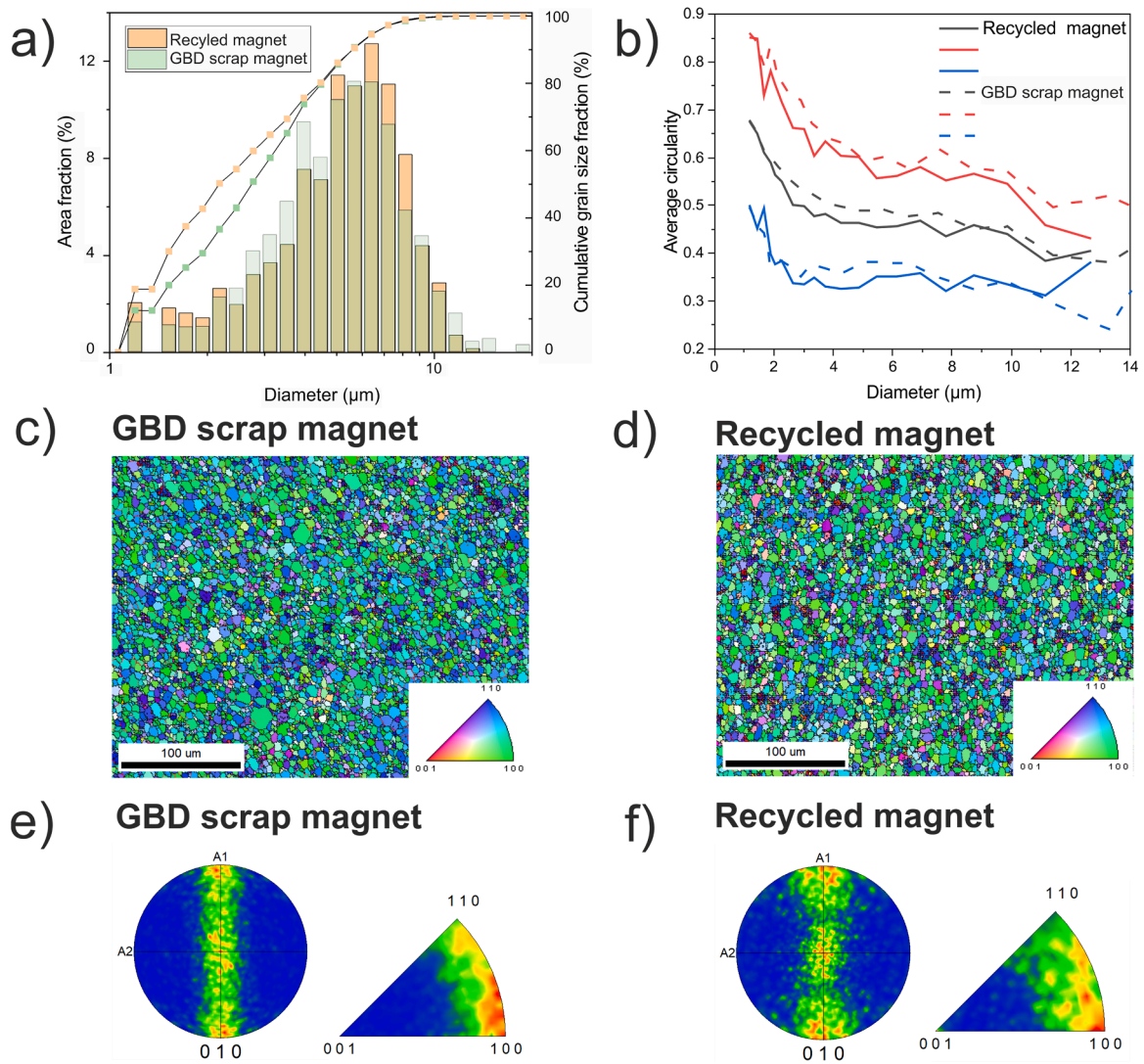
Fig. 8. a) Area fraction and frequency plots of the grain size distribution within the investigated GBD scrap and recycled magnets presented in a bar and curve plot, respectively. b) Average circularity of the GBD scrap (dashed lines) and recycled (full lines) magnets. The red and blue curves correspond to the maximum and minimum deviation of the average circularity of the grains, respectively. c) and d) present IPF maps of scrap and recycled magnet, respectively. In the lower right corner, the color wheel for the different orientations is displayed with respect to the [001] direction. e) and f) show the {010} PF projections and [001] IPF projections for GBD scrap and recycled magnet, respectively.

grain size frequency plot in Fig. 8a that displays a different fractioning of the grains in terms of their size up to 5 μm in diameter between the scrap and the recycled magnet. As a result, the overall average grain diameter of the recycled magnet is slightly lower (2.93 μm) compared to the GBD scrap magnet (3.21 μm). However, the grain size distribution spreads differently than the area fraction with respect to the individual grain size groups. As can be seen from Fig. 8a, the GBD scrap magnet presents a higher area fraction for grains of 2.5 - 4.5 μm size as well as for grains above 10 μm compared to the recycled magnet. The grain size distribution and area fraction indicate that the recycled magnet exhibits a finer microstructure with a more homogenous distribution profile compared to the corresponding values of the GBD scrap magnet. These variations can be explained by the different particle size distribution of the used powders after milling. In general, the grain refinement from the recycling process has a slight impact on the average shape of the Nd-Fe-B grains, as seen from Fig. 8b. The recycled magnet grains display on average a lower circularity (indicating how close the grain shape fits to a perfect circle, with 1 representing a perfect circular shape and 0 being a square) across all grain sizes compared to the grains from the GBD scrap magnet, which could potentially be correlated to a slight

crystallographic texturing and/or misalignment of the grains.

The crystallographic textures of the materials have been analyzed via pole figures (PF), inverse pole figures (IPF) and crystallographic orientation distribution functions (ODF) for both types of samples (Figs. 8c-f and 9). The overall IPF maps show that the recycled magnet has a wider crystallographic texture spread diverting from the general orientation of the preferred alignment with the magnetization axes (designated here as ⟨110⟩ and ⟨100⟩ by the green and blue colors). This is also revealed by the broadening of the projected pole density distribution from the {010} PF projections as well as from the [001] IPF projections that show a spread of the texture towards the [001] direction. Overall, the EBSD analysis indicates that the recycling process affects both, the grain size as well as the average misorientation of the Nd-Fe-B grains in comparison to the prior state of the scrap magnet, a result which confirms previous observations [16].

Since the IPFs and the PFs are only two-dimensional projections of the actual three-dimensional crystallographic texture, we also calculated the corresponding orientation distribution functions (ODF) for a more quantitative analysis of the differences between the two types of samples (scrap and recycled magnet), which is shown in Fig. 9. The
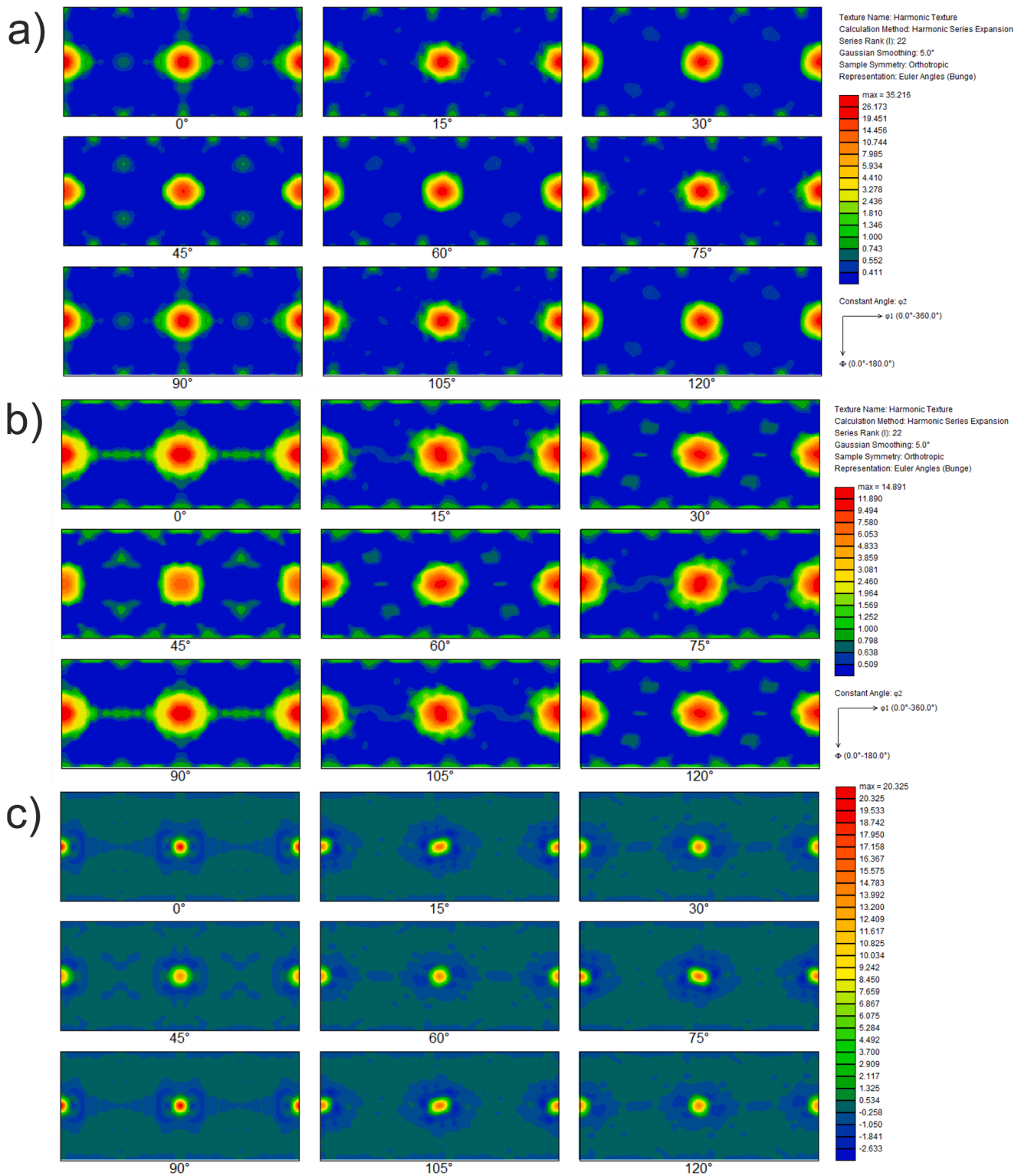
Fig. 9. Orientation density function (ODF) plots of the a) GBD scrap magnet and b) recycled magnet that are plotted with 15° steps of the Φ angle. In c) the plots represent the difference of the ODF plots of the GBD scrap magnet versus recycled magnet, i.e. ODF$_{scrap}$-ODF$_{recycled}$.

ODFs have been calculated here through a series expansion method using symmetrized spherical harmonic library functions, and they are plotted here in the form of sections through the symmetry-reduced Euler space. This ODF analysis of the two types of materials indeed reveals a profound orientation spread of the recycled magnet away from the alignment axis compared to the GBD scrap magnet, differing by nearly a factor of 2 in the orientation density (seen from the maximum orientation density values along the (100) direction), as shown in Fig. 9a-c. This is also shown in the fiber texture plot for the Φ = 0° orientation density distribution section provided in Fig. 10. This figure clearly displays the nearly factor of 2 higher divergences of the orientation from the main alignment axis for the recycled magnet in comparison to the GBD scrap magnet. Correspondingly, the difference plot in Fig. 9c shows that the major divergence of the grains from the
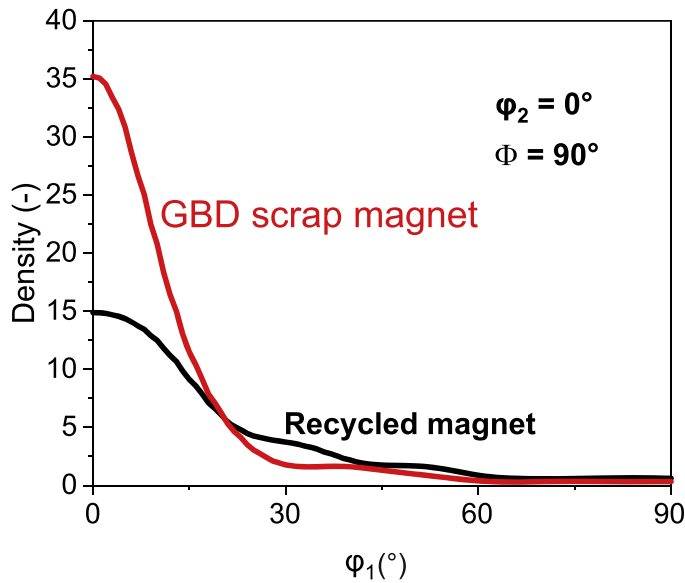
Fig. 10. Density vs Φ1 angle plot presenting the density changes from the ODF of the GBD scrap magnet and recycled magnet at set φ2 and Φ angles.

alignment axis originates from the spreading around the main axis (see blue hue around the principal (100) peaks) within the 30° range of the Φ and φ2 angles.

The ODF data for both magnets show that the divergence from the main alignment axis goes towards the (121) and (131) directions, which can be clearly seen from the Φ = 45° and Φ = 60° ODF sections from Fig. 9a and b as well as from Fig. 10. This finding requires in future deeper analysis. Possible reasons for this quite profound dissimilarity in the process-dependent crystallographic orientation distribution might lie in underlying differences in crystal nucleation and / or crystal growth mechanisms and constraints along specific directions, being both kinetic features that can occur during recrystallization and competitive

coarsening effects happening during heat treatment and sintering [58].

To investigate the change in Tb-shell thickness, the GBD scrap magnets were annealed at different temperatures under vacuum. Fig. 11 shows the SEM BSE images of these microstructures. After 500 °C for 1 h the Tb-shells are still visible at the edges of the grains. However, after annealing at 700 °C, 900 °C or 1100 °C for 1 h, the shells are less clear visible.

Like in the case of recycled magnets, EDS line scans also reveal a broadening or smearing of the shells, as shown in Fig. 12. After annealing at 500 °C the magnet shows also 0.5 μm thick shells which increases to 1.0 μm after annealing at 1100 °C. Note that the sintering at 1100 °C with subsequent low-temperature annealing at 700 °C and 500 °C during the recycling process takes in total 6 h.

The observed microstructural changes are the reason for the decrease in coercivity discussed in Section 3.2. The formation of a $(Nd,HRE)_2$-$Fe_{14}B$ shell with higher magnetocrystalline anisotropy leads to a magnetic hardening effect and increases the resistance against the nucleation of reversed magnetic domains [4,59]. Without the presence of these distinct shells, the demagnetization starts already at lower magnetic fields at regions with lower local magnetocrystalline anisotropy as in the grain boundaries, edges of grains and imperfections, leading to a reduced coercivity of the recycled and annealed magnets. The formation of reversed magnetic domains is also supported by local demagnetization fields which have their maximum at the edges and corners of the grains. Microstructural magnetic inhomogeneities in Nd-Fe-B sintered magnets lead to differences between the ideal and the real nucleation field, which is also known as Brown's paradox. To better understand the influence of defects on the coercive field H_C in magnets, the following equation according to Kronmüller [60,61] can be used

$$H_c(T) = \gamma(T)\frac{2K_1}{M_S} - N_{eff}M_S(T) \qquad (6)$$

where γ is a microstructural parameter that quantifies the reduction of the coercive field by soft magnetic defects, K_1 the first anisotropy constant and M_S the spontaneous magnetization. M_S is an intrinsic magnetic property which depends on the composition of the magnet and on the
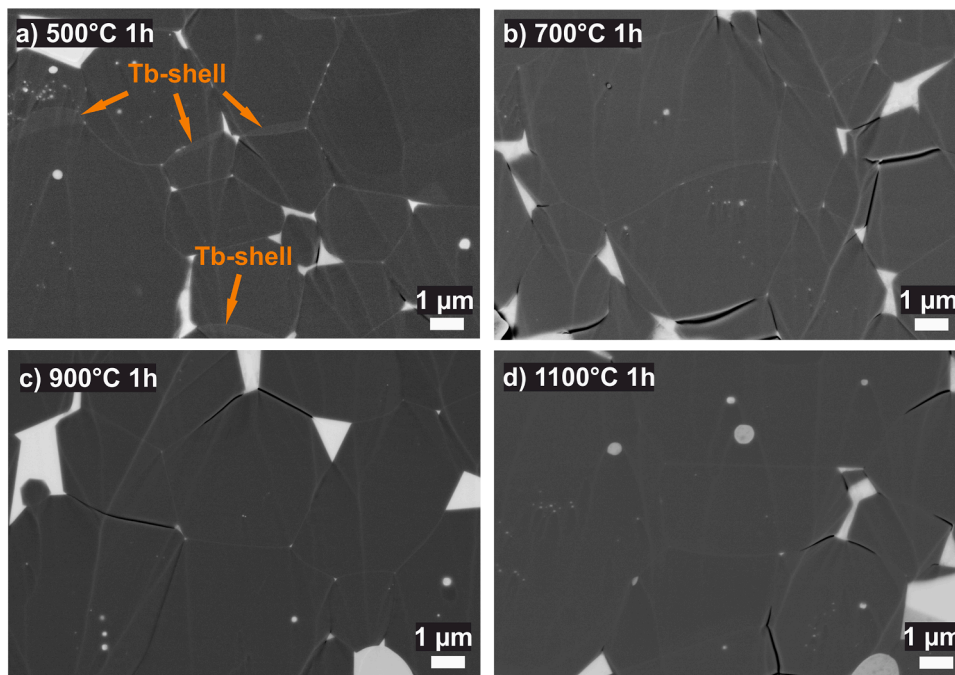

Fig. 11. SEM BSE images of the GBD scrap magnets after annealing under vacuum at 500 °C (a), 700 °C (b), 900 °C (c) and 1100 °C (d). The Tb-shell is still clear visible after annealing at 500 °C for 1 h, but less clear visible after annealing at higher temperatures. All images were taken at a distance of 200 - 300 μm from the surface.
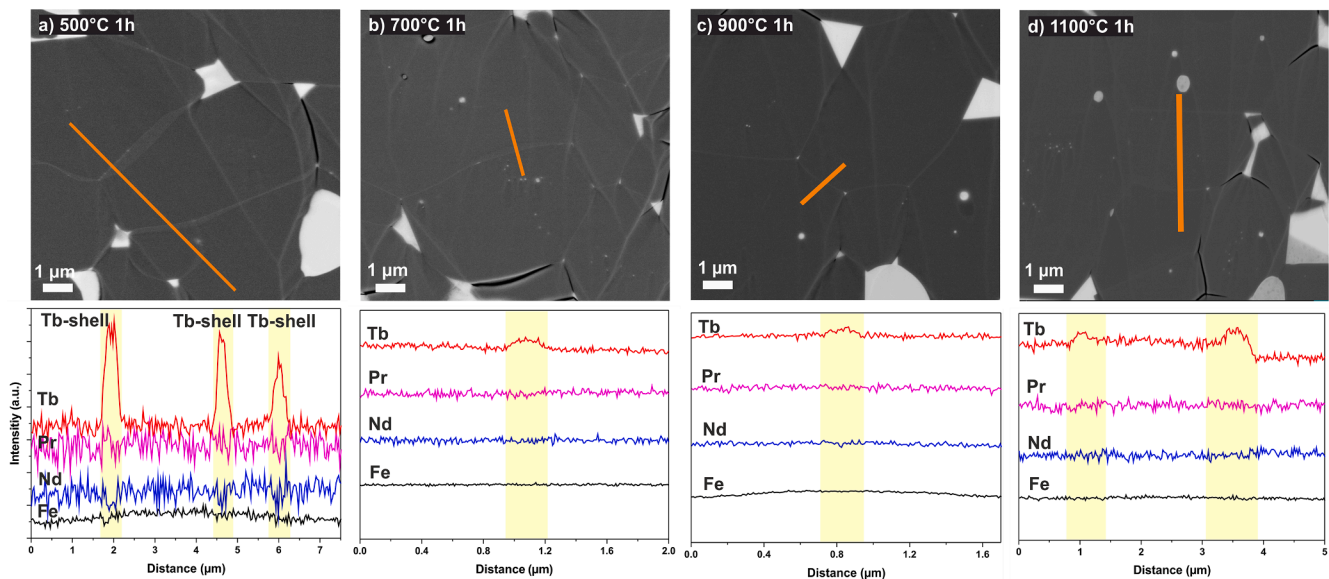
Fig. 12. EDS line scans of annealed GBD scrap magnets show a broadening of Tb-shells from 0.5 μm to 1.0 μm through annealing at higher temperatures. All line scans were done at a distance of 200 - 300 μm from the surface. For comparability, the intensities of the EDS line scans are normalized.

temperature T. N_{eff} is a local effective demagnetization factor which brings the effect of demagnetization fields into account. Helbig *et al.* [62] analyzed the magnetization reversal in core-shell sintered magnets in detail. It was found that the coercivity has a strong dependency on the magnetocrystalline anisotropy at the shell surface K^{edge}. Small K^{edge} values result in a nucleation of the magnetization reversal at the shell surface, while higher values cause a shift of the nucleation site to the core of the grain. Micromagnetic simulations from Fischbacher *et al.* [63] also showed, that the improvement of coercivity through the formation of $(Nd,Dy)_2Fe_{14}B$ shells is associated with a shift of those microstructure sites, which act as spots at which the magnetization reversal starts through nucleation of reversed domains. In a magnet without HRE shells, the magnetization reversal through nucleation starts at the grain boundaries at the outer edge of the magnet. After formation of HRE-shells, e.g. through GBD, the weakest microstructure site, where demagnetization is initiated, shifts towards the center of the sample. First, nucleation then typically occurs at a grain boundary junction in the middle of the magnet (only surface grains are covered with HRE-shells), then it moves inside to the center of the grains (all grains are covered with HRE-shells). Recently, Li *et al.* [64] published a multi-step nucleation of magnetic reversal domain process in core-shell magnets, in which the nucleation of new domains with reversed magnetization starts at the Dy-lean core region and the defect edge region successively. However, these micromagnetic simulations indicate that the observed absence of the HRE-rich shell leads to a shift of the nucleation site of reversed domains to areas with lower local magnetocrystalline anisotropy and therefore to a reduced resistance against demagnetization and reduced coercivity.

Fig. 13 shows the magneto-optical Kerr (MOKE) images and domain structure evolution through the demagnetization process of the GBD scrap magnet and of the recycled magnet along the easy magnetization axis. In thermally demagnetized state, a homogenous microstructure with most of the grains showing typical maze-like domains can be observed, demonstrating a well aligned texture. It is worth mentioning that some grains on the recycled magnet are misoriented, as denoted by the stripe domains highlighted by the red arrows, which explains their contribution to the lower remanence observed in this magnet compared to the original one. After application of a 7 T magnetic field pulse (saturation), nearly all grains are in saturated state - showing only one contrast. However, a few grains (highlighted with white arrows) show a multidomain state, indicating an already partial demagnetization in

some regions, being more pronounced in the recycled magnet. These can be attributed to the lower nucleation field in these grains [60,65]. The grains showing a multidomain state increases after a magnetic field of 1 T has been applied in the opposite direction relative to the saturation direction. Qualitatively, a larger portion of the recycled magnet is demagnetized compared to the GBD scrap magnet. A similar trend is seen when the applied field is increased to 2 T, where the number of grains in multidomain state increases for the GBD scrap magnet while fully reversed grains are already observed for the recycled magnet, which is represented by the inverted contrast compared to the initial saturated state. Only with further increase in the applied magnetic field to 3 T, grains with reversed magnetization are visible in the GBD scrap magnet along with grains in multidomain state. At this same condition, a substantial portion of the observed area of 110×70 μm of the recycled magnet is showing grains with fully reversed magnetization. As an overall observation, the nucleation and growth of reversed domains is hindered in the GBD scrap magnet, while nucleation in the recycled magnet takes place already at lower applied magnetic fields, in agreement with the demagnetizing curves shown in Fig. 2. This behavior could be explained by the presence of a more pronounced core-shell microstructure in the GBD scrap magnet, which increases the nucleation field of reversal magnetic domains. A similar behavior was also reported by Liu *et al.* and Wu *et al.* [66,67]. They observed a transformation of the magnetic domain reversal mode from easy nucleation (gradual reversal) to difficult nucleation (abrupt reversal) through the formation of Tb-rich shells.

3.4. Grain boundary diffusion at recycled magnets

To improve the magnetic properties of the recycled magnets, a new GBD process was applied on the recycled magnets to form a renewed core-shell structure (see Fig. 14). The thickness of the Tb-shells near the surface is $0.5 – 0.6$ μm which is comparable to the shells of the GBD scrap magnets (0.5 μm). Through EDS line scans it is possible to observe a reduction of Nd by Tb substitution and formation of $(Nd,Tb)_2Fe_{14}B$ shells.

Fig. 15 shows the temperature dependent magnetic properties of the GBD scrap magnet, of the recycled magnet and of the recycled magnet after the renewed GBD. In case of the GBD scrap magnet and the recycled magnet, rectangular demagnetization curves can be observed. After the applied Tb-GBD, the recycled magnet shows a less rectangular
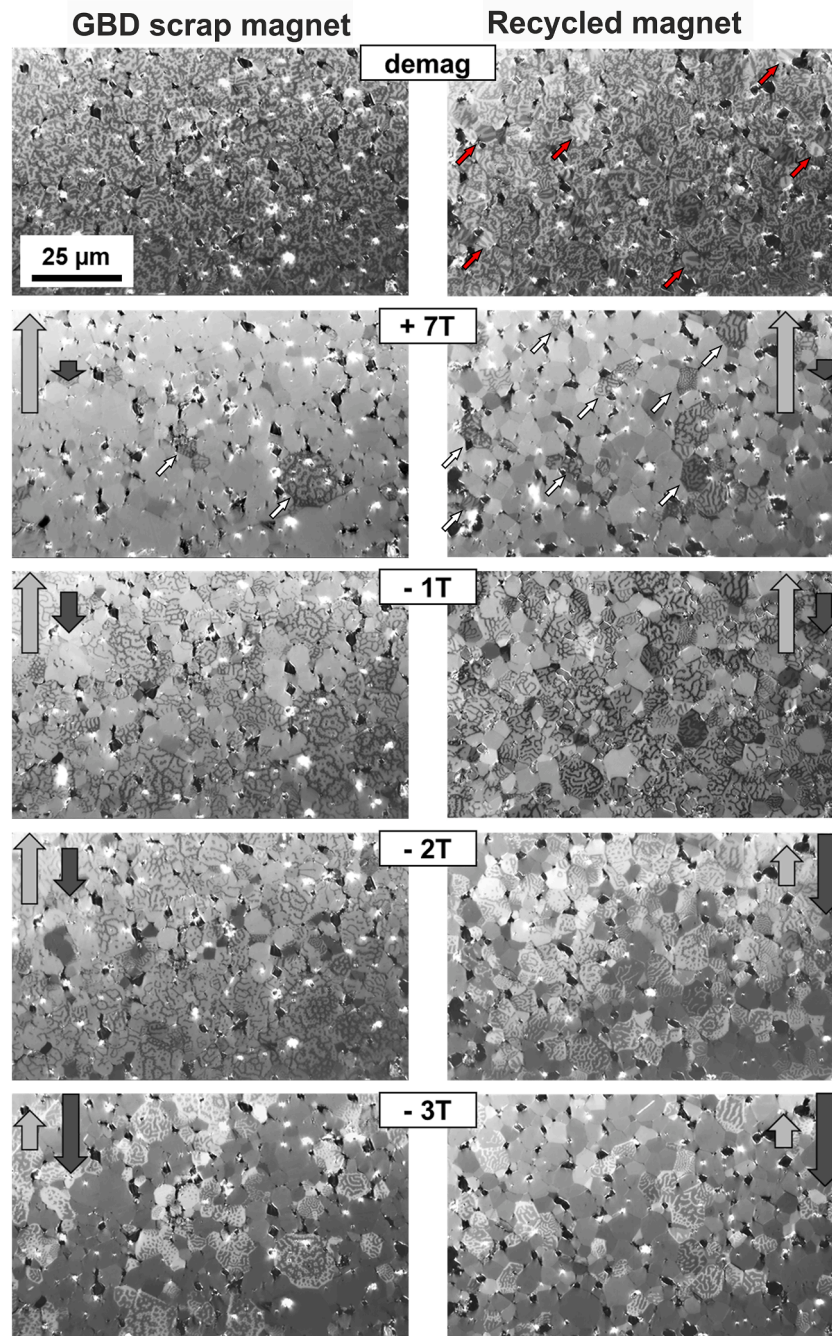
Fig. 13. MOKE images of the magnetic domain evolution of a GBD scrap magnet and of a recycled magnet during demagnetization at different field strengths starting from their respective demagnetized states. The two arrows in the left upper corner qualitatively indicate the magnetization of the observed area. The light grey arrow indicates the direction of the saturation field (+7 T) and the dark grey arrow represents the grains with reversed magnetization. The sample was prepared with the easy magnetization axis pointing out of plane.

demagnetization curve. This is due to an inhomogeneous distribution of Tb from the surface of the magnet to the center. Reasons for the inhomogeneous distribution are the non-optimized GBD (Tb content, heat treatment) and the relatively large height of 6.47 mm of the recycled magnets when compared to the GBD scrap magnet (5.3 mm). In general, the typical height of GBD magnets should not exceed 5 mm to prevent negative effects related to inhomogeneous distribution of HRE elements [68,69]. Possible methods to produce thick magnets with reduced HRE content and a core-shell structure are the so-called dual-alloy method [70] or the 2-powder-method [43,71–73] whereby the diffusion of HRE elements takes place from the inner region of the magnet and not from the surface.

The remanence (Fig. 15d) and coercivity (Fig. 15e) of the recycled magnet decreases through the functional recycling process by 5 % and 21 %, respectively. The reasons are the discussed nearly 2 times higher deviation of the grains from the alignment axis, impurity uptake and changes in microstructure (see Sections 3.2 and 3.3). The new GBD has only a small influence on the remanence, but a larger one on the coercivity of the magnets, corroborating to the influence of the short-range exchange coupling between grains. Through the formation of new Tb-shells, the coercivity of recycled magnet is increased by 35 % from 1315 kA/m to 1780 kA/m at 50 °C and shows similar values as the GBD scrap magnet at 150 °C or 200 °C. With the process used here (application of 1.5 wt.% Tb foil to the magnetic surface), an H_{cJ} increase of 465
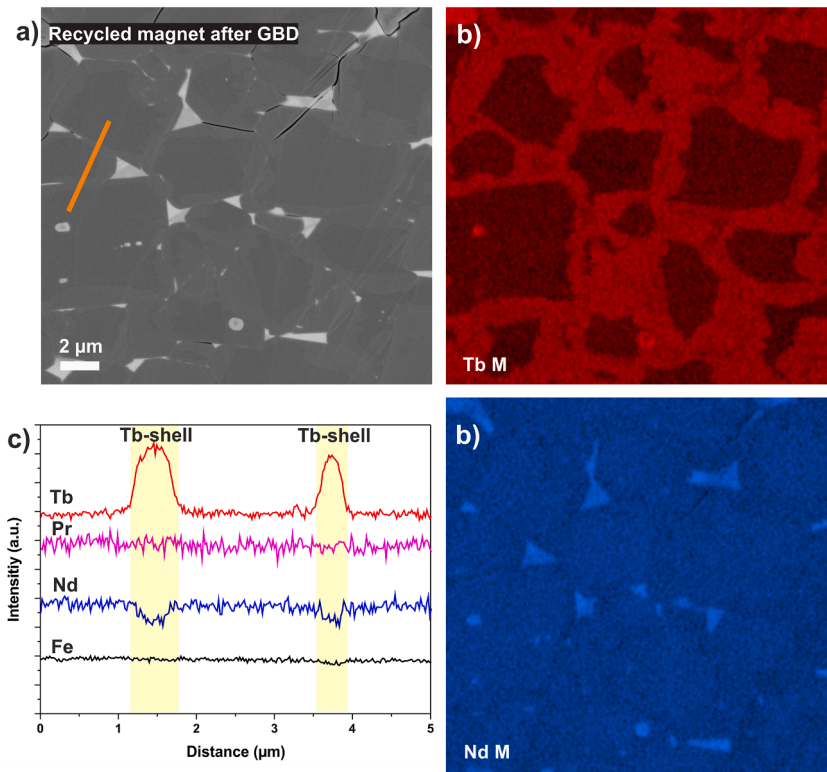
Fig. 14. SEM BSE image (a) and EDS mappings (b) of a recycled magnet after a renewed GBD process. A new formation of Tb-shells is clear visible. The thickness of the Tb-shells is determined with EDS line scans (c) to 0.5 - 0.6 μm which is comparable to the GBD scrap magnet.
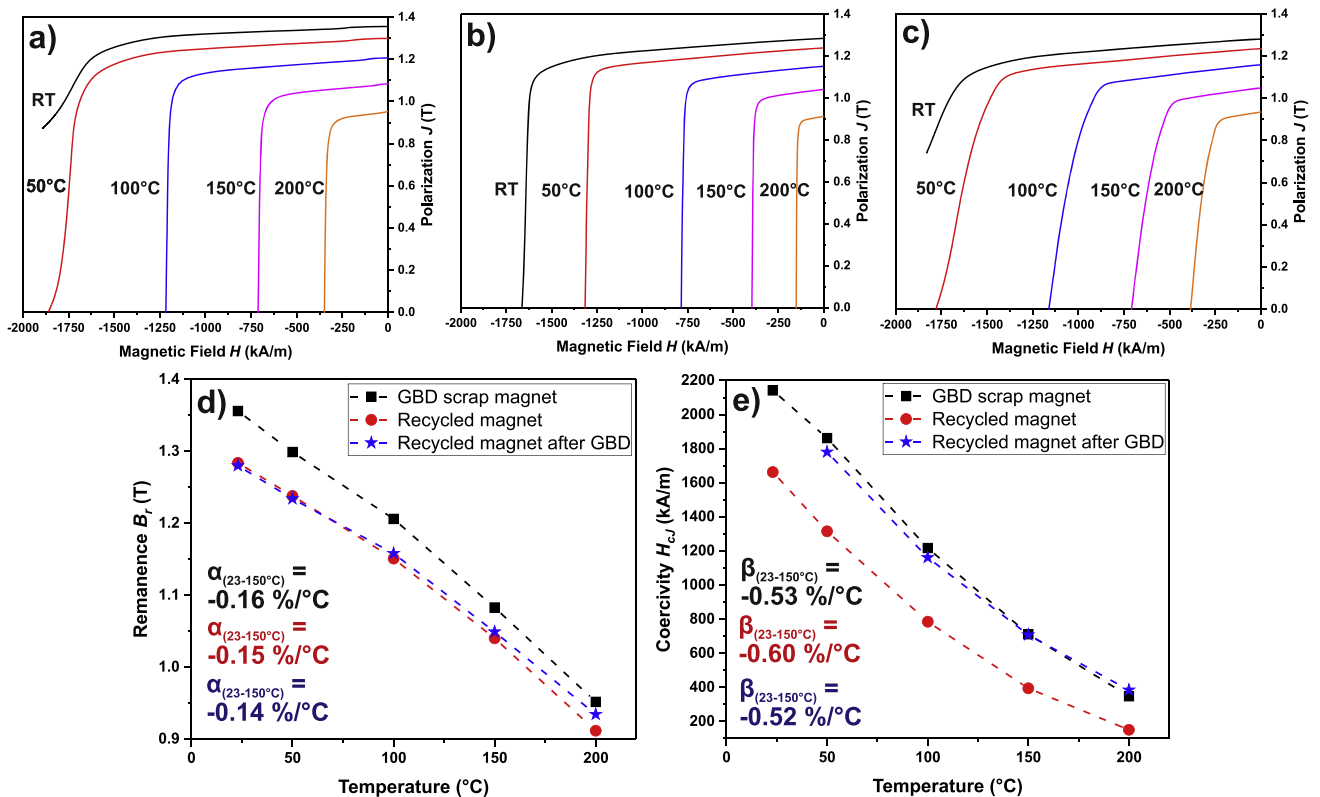

Fig. 15. Demagnetization curves of the GBD scrap magnet (a), recycled magnet (b), and recycled magnet after renewed GBD (c), and remanence (d) and coercivity (e) of all three magnets in dependence of applied temperature. After the renewed GBD the coercivity of recycled magnets can be fully restored. Note that in a) and c), the coercivity value at RT is higher than the limit of the applied field in the hysteresis graph.

kA/m at 50 °C was achieved. The achievable H_{cJ} increase depends on the amount of Tb actually present in the magnet, which is less than the 1.5 wt.% applied to the surface. Furthermore, the application of the HRE (sputtering, HRE-suspension, bulk material or foil) plays an important role in the GBD process and thus also for the achievable H_{cJ} increase, as does the thickness of the coated magnet [33]. The dissimilar temperature evolution of the demagnetization curves in terms of the shape and coercivity between GBD scrap magnet and recycled magnet after GBD instigates a possible cross-coupling of the magnetic properties to the chemical and crystallographic features and spatial distribution of them within the recycled magnet. The mass density of the recycled magnets can be also improved to 7.57 g/cm^3 (7.53 g/cm^3 before GBD) through the addition of HRE. Figs. 15d and e show also the calculated temperature coefficients for the remanence, α, and for the coercivity, β, of all three magnets. In the temperature range between 23 °C and 150 °C α amounts to -0.16 %/ °C and β to -0.53 %/ °C which are both typical values for sintered Nd-Fe-B magnets [74,75]. In case of the recycled magnets, the temperature coefficient of coercivity is more affected through the observed changes in microstructure and decreases to -0.60 %/ °C while α shows a minimal increase of 0.01 %/ °C. However, through the restoring of the core-shell microstructure, both values can be fully restored and exceed the original values which leads to an improved temperature stability of recycled magnets compared to the primary GBD scrap magnets.

4. Summary and conclusions

It was shown by microstructure and chemical characterization, from the mesoscale down to near-atomic scale, that the functional recycling of GBD magnets leads to a dissolution of the core-shell structure through the heat treatments at the hydrogen decrepitation, sintering and annealing processing steps. While the starting material shows a squareness SQ of 96 %, remanence B_r of 1.38 T, and coercivity H_{cJ} of 2143 kA/m, the recycled magnet has the same SQ of 96 %, with a slightly decreased B_r of 1.31 T, but a larger decrease in H_{cJ} of 21 % to 1703 kA/m. The heat-treatment related smearing of the core-shell structure could be the reason for the reduction of H_{cJ}. In addition, the crystallographic texture of the recycled magnet presents a nearly 2-times higher divergence from the main alignment axis, which can be correlated to the reduced B_r. A renewed GBD with 1.5 wt.% Tb leads again to a formation of core-shell structure with 0.5 μm thick Tb-shells at the outer region of the grains which is similar to the microstructure of the GBD scrap magnets. The coercivity of the recycled magnets is increased by 35 % from 1315 kA/m to 1780 kA/m at 50 °C and shows similar values as the GBD scrap magnet exposed to 150 °C or 200 °C, respectively. The temperature coefficients α and β can be fully restored and exceed the original values which leads to an improved temperature stability of recycled magnets compared to the primary GBD scrap magnets. The functional recycling has thus led to a clear difference in the magnetic properties compared to the GBD scrap magnet, as a result of the combination of crystallographic, microstructural and chemical changes of the material. To provide further insight into the limitations and main influencing factors affecting functional recycling of GBD magnets, correlative and/or in-situ measurements of the recycled magnets by decoupling the individual influencing factors could be utilized in the future.

We have shown that with the functional recycling approach it is possible to recycle commercial GBD magnets with good resulting magnetic properties and rectangular demagnetization curves. To compensate and restore the microstructure induced coercivity losses a new GBD process with HREs has been introduced and tested successfully. The use of additional HRE elements will to some extend harm the sustainability of these materials, but such recycled magnets are still far more sustainable than magnets made from primary production.

CRediT authorship contribution statement

Mario Schönfeldt: Writing – original draft, Visualization, Validation, Methodology, Investigation, Conceptualization. **Jürgen Rossa:** Validation, Methodology, Investigation. **Konrad Opelt:** Writing – original draft, Methodology, Conceptualization. **Kilian Schäfer:** Writing – original draft, Visualization, Validation, Investigation. **Lukas Schäfer:** Writing – original draft, Visualization, Validation, Investigation. **Fernando Maccari:** Writing – original draft, Visualization, Validation, Investigation. **Matic Jovičević-Klug:** Writing – original draft, Visualization, Validation, Methodology, Investigation. **Tim M. Schwarz:** Writing – original draft, Visualization, Validation, Methodology, Investigation. **Chi-Chia Lin:** Validation, Investigation. **Mahmudul Hasan:** Validation, Investigation. **Jürgen Gassmann:** Writing – review & editing, Supervision, Methodology, Funding acquisition. **Dierk Raabe:** Writing – review & editing, Supervision, Methodology, Funding acquisition, Conceptualization. **Oliver Gutfleisch:** Writing – review & editing, Supervision, Methodology, Funding acquisition, Conceptualization.

Declaration of competing interest

The authors declare that they have no known competing financial interests or personal relationships that could have appeared to influence the work reported in this paper.

Supplementary materials

Supplementary material associated with this article can be found, in the online version, at doi:10.1016/j.actamat.2024.120532.

References

[1] Roland Gauß, Carlo Burkhardt, Frédéric Carencotte, Massimo Gasparon, Oliver Gutfleisch, Ian Higgins, Milana Karajić, Andreas Klossek, Maija Mäkinen, Bernd Schäfer, Reinhold Schindler, Badrinath Veluri, Rare Earth Magnets and Motors: A European Call for Action. A report by the Rare Earth Magnets and Motors Cluster of the European Raw Materials Alliance, 2021. Berlin.

[2] O. Gutfleisch, M.A. Willard, E. Brück, C.H. Chen, S.G. Sankar, J.P. Liu, Magnetic materials and devices for the 21st century: stronger, lighter, and more energy efficient, Adv. Mater. (Deerfield Beach, Fla.) 23 (2011) 821–842, https://doi.org/10.1002/adma.201002180.

[3] Adamas Intelligence, Rare earth magnet market outlook to 2035, 2022.

[4] F. Chen, Recent progress of grain boundary diffusion process of Nd-Fe-B magnets, J. Magn. Magn. Mater. 514 (2020) 167227, https://doi.org/10.1016/j.jmmm.2020.167227.

[5] Y. Geng, J. Sarkis, R. Bleischwitz, How to build a circular economy for rare-earth elements, Nature 619 (2023) 248–251, https://doi.org/10.1038/d41586-023-02153-z.

[6] P. Zapp, A. Schreiber, J. Marx, W. Kuckshinrichs, Environmental impacts of rare earth production, MRS Bull. 47 (2022) 267–275, https://doi.org/10.1557/s43577-022-00286-6.

[7] A. Kumari, S.K. Sahu, A comprehensive review on recycling of critical raw materials from spent neodymium iron boron (NdFeB) magnet, Sep. Purif. Technol. 317 (2023) 123527, https://doi.org/10.1016/j.seppur.2023.123527.

[8] H. Jin, P. Afiuny, S. Dove, G. Furlan, M. Zakotnik, Y. Yih, J.W. Sutherland, Life cycle assessment of neodymium-iron-boron magnet-to-magnet recycling for electric vehicle motors, Environ. Sci. Technol. 52 (2018) 3796–3802, https://doi.org/10.1021/acs.est.7b05442.

[9] J.H. Rademaker, R. Kleijn, Y. Yang, Recycling as a strategy against rare earth element criticality: a systemic evaluation of the potential yield of NdFeB magnet recycling, Environ. Sci. Technol. 47 (2013) 10129–10136, https://doi.org/10.1021/es305007w.

[10] B. Sprecher, Y. Xiao, A. Walton, J. Speight, R. Harris, R. Kleijn, G. Visser, G. J. Kramer, Life cycle inventory of the production of rare earths and the subsequent production of NdFeB rare earth permanent magnets, Environ. Sci. Technol. 48 (2014) 3951–3958, https://doi.org/10.1021/es404596q.

[11] K. Binnemans, P.T. Jones, B. Blanpain, T. van Gerven, Y. Yang, A. Walton, M. Buchert, Recycling of rare earths: a critical review, J. Clean. Prod. 51 (2013) 1–22, https://doi.org/10.1016/j.jclepro.2012.12.037.

[12] Y. Yang, A. Walton, R. Sheridan, K. Güth, R. Gauß, O. Gutfleisch, M. Buchert, B.-M. Steenari, T. van Gerven, P.T. Jones, K. Binnemans, REE recovery from End-of-Life NdFeB permanent magnet scrap: a critical review, J. Sustain. Metall. 3 (2017) 122–149, https://doi.org/10.1007/s40831-016-0090-4.

[13] A. Habibzadeh, M.A. Kucuker, M. Gökelma, Review on the parameters of Recycling NdFeB magnets via a hydrogenation process, ACS. Omega 8 (2023) 17431–17445, https://doi.org/10.1021/acsomega.3c00299.

[14] O. Gutfleisch, K. Güth, T.G. Woodcock, L. Schultz, Recycling used Nd-Fe-B sintered magnets via a hydrogen-based route to produce anisotropic, resin bonded magnets, Adv. Energy Mater. 3 (2013) 151–155, https://doi.org/10.1002/aenm.201200337.

[15] O. Diehl, M. Schönfeldt, E. Brouwer, A. Dirks, K. Rachut, J. Gassmann, K. Güth, A. Buckow, R. Gauß, R. Stauber, O. Gutfleisch, Towards an alloy recycling of Nd–Fe–B permanent magnets in a circular economy, J. Sustain. Metall. 4 (2018) 163–175, https://doi.org/10.1007/s40831-018-0171-7.

[16] M. Schönfeldt, U. Rohrmann, P. Schreyer, M. Hasan, K. Opelt, J. Gassmann, A. Weidenkaff, O. Gutfleisch, Magnetic and structural properties of multiple recycled and sustainable sintered Nd-Fe-B magnets, J. Alloys. Compd. 939 (2023) 168709, https://doi.org/10.1016/j.jallcom.2023.168709.

[17] I. Husain, B. Ozpineci, M.S. Islam, E. Gurpinar, G.-J. Su, W. Yu, S. Chowdhury, L. Xue, D. Rahman, R. Sahu, Electric drive technology trends, challenges, and opportunities for future electric vehicles, Proc. IEEE 109 (2021) 1039–1059, https://doi.org/10.1109/JPROC.2020.3046112.

[18] H. Nakamura, The current and future status of rare earth permanent magnets, Scr. Mater. 154 (2018) 273–276, https://doi.org/10.1016/j.scriptamat.2017.11.010.

[19] K.T. Park, K. Hiraga, M. Sagawa, Effect of metal-coating and consecutive heat treatment on coercivity of thin Nd-Fe-B sintered magnets, in: Proceedings of 16th International Workshop on Rare Earth Magnets and Their Applications, 2000.

[20] K.-H. Müller, S. Sawatzki, R. Gauß, O. Gutfleisch, Permanent magnet materials, in: M. Coey, S. Parkin (Eds.), Handbook of Magnetism and Magnetic Materials, Springer International Publishing, Cham, 2020, pp. 1–65.

[21] G. Hrkac, T.G. Woodcock, C. Freeman, A. Goncharov, J. Dean, T. Schrefl, O. Gutfleisch, The role of local anisotropy profiles at grain boundaries on the coercivity of Nd2Fe14B magnets, Appl. Phys. Lett. 97 (2010), https://doi.org/10.1063/1.3519906.

[22] H. Sepehri-Amin, T. Ohkubo, K. Hono, Grain boundary structure and chemistry of Dy-diffusion processed Nd–Fe–B sintered magnets, J. Appl. Phys. 107 (2010), https://doi.org/10.1063/1.3351247.

[23] X. Cao, L. Chen, S. Guo, R. Chen, G. Yan, A. Yan, Impact of TbF3 diffusion on coercivity and microstructure in sintered Nd–Fe–B magnets by electrophoretic deposition, Scr. Mater. 116 (2016) 40–43, https://doi.org/10.1016/j.scriptamat.2016.01.034.

[24] T. Zhou, R. Liu, P. Qu, Q. Xie, M. Li, Z. Zhong, Diffusion behavior and coercivity enhancement of Tb-containing NdFeB magnet by dip-coating TbH3, J. Mater. Res. Technol. 20 (2022) 1391–1398, https://doi.org/10.1016/j.jmrt.2022.07.167.

[25] M. Itakura, M. Namura, M. Nishida, H. Nakamura, Elemental distribution near the grain boundary in a Nd–Fe–B sintered magnet subjected to grain-boundary diffusion with Dy2O3, Mater. Trans. 61 (2020) 438–443, https://doi.org/10.2320/matertrans.MT-M2019265.

[26] S. Cao, X. Bao, J. Li, H. Yu, K. Zhu, X. Gao, Improvement of microstructure and coercivity for Nd-Fe-B sintered magnets by boundary introducing low melting point alloys, J. Rare Earths 38 (2020) 395–401, https://doi.org/10.1016/j.jre.2019.04.021.

[27] T. Zhou, Y. Guo, G. Xie, S.U. Rehman, R. Liu, J. Liu, P. Qu, M. Li, Coercivity and thermal stability enhancement of NdFeB magnet by grain boundary diffusion Tb80Al20 alloys, Intermetallics. (Barking) 138 (2021) 107335, https://doi.org/10.1016/j.intermet.2021.107335.

[28] W. Chen, J.M. Luo, Y.W. Guan, Y.L. Huang, M. Chen, Y.H. Hou, Grain boundary diffusion of Dy films prepared by magnetron sputtering for sintered Nd–Fe–B magnets, J. Phys. D: Appl. Phys. 51 (2018) 185001, https://doi.org/10.1088/1361-6463/aab912.

[29] U. Seelam, T. Ohkubo, T. Abe, S. Hirosawa, K. Hono, Faceted shell structure in grain boundary diffusion-processed sintered Nd–Fe–B magnets, J. Alloys. Compd. 617 (2014) 884–892, https://doi.org/10.1016/j.jallcom.2014.07.166.

[30] W. Zhu, Y. Luo, Z. Wang, X. Bai, H. Peng, D. Yu, Magnetic properties and microstructures of terbium coated and grain boundary diffusion treated sintered Nd-Fe-B magnets by magnetron sputtering, J. Rare Earths 39 (2021) 167–173, https://doi.org/10.1016/j.jre.2020.02.017.

[31] B. Wu, Q. Zhang, W. Li, X. Ding, L. Yang, A. Ghafar Wattoo, L. Zhang, S. Mao, Z. Song, Grain boundary diffusion of magnetron sputter coated heavy rare earth elements in sintered Nd-Fe-B magnet, J. Appl. Phys. 123 (2018), https://doi.org/10.1063/1.5023092.

[32] K. Loewe, D. Benke, C. Kübel, T. Lienig, K.P. Skokov, O. Gutfleisch, Grain boundary diffusion of different rare earth elements in Nd-Fe-B sintered magnets by experiment and FEM simulation, Acta Mater. 124 (2017) 421–429, https://doi.org/10.1016/j.actamat.2016.11.034.

[33] Z. Liu, J. He, R.V. Ramanujan, Significant progress of grain boundary diffusion process for cost-effective rare earth permanent magnets: A review, Mater. Des. 209 (2021) 110004, https://doi.org/10.1016/j.matdes.2021.110004.

[34] B. Wu, X. Ding, Q. Zhang, L. Yang, B. Zheng, F. Hu, Z. Song, The dual trend of diffusion of heavy rare earth elements during the grain boundary diffusion process for sintered Nd-Fe-B magnets, Scr. Mater. 148 (2018) 29–32, https://doi.org/10.1016/j.scriptamat.2018.01.021.

[35] Z. Toujun, W. Bao, Z. Xu, M. Zhao, X. Huang, W. Wei, R. Liu, G. Xie, Optimizing microstructure, magnetic properties and mechanical properties of sintered NdFeB magnet by double alloy method and grain boundary diffusion, Intermetallics. (Barking) 162 (2023) 108027, https://doi.org/10.1016/j.intermet.2023.108027.

[36] T. Zhou, J. Chen, Q. Wang, W. Pan, Q. Huang, R. Liu, M. Li, G. Xie, Super-high coercivity NdFeB magnet fabricated with double Tb-rich/lean shells by double alloy method and grain boundary diffusion, J. Alloys. Compd. 937 (2023) 168368, https://doi.org/10.1016/j.jallcom.2022.168368.

[37] T. Zhou, P. Qu, W. Pan, R. Liu, M. Li, S.U. Rehman, Z. Zhong, G. Xie, Sintered NdFeB magnets with Tb - Dy double-layer core/shell structure were fabricated by double alloy method and grain boundary diffusion, J. Alloys. Compd. 856 (2021) 158191, https://doi.org/10.1016/j.jallcom.2020.158191.

[38] I. Dirba, P. Pattur, I. Soldatov, E. Adabifiroozjaei, L. Molina-Luna, O. Gutfleisch, Grain boundary infiltration in HDDR processed Nd2Fe14B magnets, J. Alloys. Compd. 930 (2023) 167411, https://doi.org/10.1016/j.jallcom.2022.167411.

[39] Z. Liu, J. He, Q. Zhou, Y. Huang, Q. Jiang, Development of non-rare earth grain boundary modification techniques for Nd-Fe-B permanent magnets, J. Mater. Sci. Technol. 98 (2022) 51–61, https://doi.org/10.1016/j.jmst.2021.05.012.

[40] Y. Liu, J. He, H. Yu, Z. Liu, G. Zhang, Restoring and enhancing the coercivity of waste sintered (Nd,Ce,Gd)FeB magnets by direct Pr–Tb–Cu grain boundary diffusion, Appl. Phys. A: Mater. Sci. Process. 126 (2020), https://doi.org/10.1007/s00339-020-03857-z.

[41] W. Ji, W. Liu, M. Yue, D. Zhang, J. Zhang, Coercivity enhancement of recycled Nd–Fe–B sintered magnets by grain boundary diffusion with DyH3 nano-particles, Physica B: Condensed Matter 476 (2015) 147–149, https://doi.org/10.1016/j.physb.2015.03.013.

[42] H. Sepehri-Amin, T. Ohkubo, M. Zakotnik, D. Prosperi, P. Afiuny, C.O. Tudor, K. Hono, Microstructure and magnetic properties of grain boundary modified recycled Nd-Fe-B sintered magnets, J. Alloys. Compd. 694 (2017) 175–184, https://doi.org/10.1016/j.jallcom.2016.09.305.

[43] K. Opelt, T. Ahmad, O. Diehl, M. Schönfeldt, E. Brouwer, I. Vogel, J.D. Rossa, J. Gassmann, S. Ener, O. Gutfleisch, Upscaling the 2-Powder method for the manufacturing of heavy rare-earth-lean sintered didymium-based magnets, Adv. Eng. Mater. (2021) 2100459, https://doi.org/10.1002/adem.202100459.

[44] P. Kausch, J. Matschullat, M. Bertau, H. Mischo (Eds.), Rohstoffwirtschaft und Gesellschaftliche Entwicklung: Die nächsten 50 Jahre, Springer Spektrum, Berlin, Heidelberg, 2016.

[45] O. Gutfleisch, I.R. Harris, Fundamental and practical aspects of the hydrogenation, disproportionation, desorption and recombination process, J. Phys. D: Appl. Phys. 29 (1996) 2255–2265, https://doi.org/10.1088/0022-3727/29/9/006.

[46] K. Thompson, D. Lawrence, D.J. Larson, J.D. Olson, T.F. Kelly, B. Gorman, In situ site-specific specimen preparation for atom probe tomography, Ultramicroscopy. 107 (2007) 131–139, https://doi.org/10.1016/j.ultramic.2006.06.008.

[47] T.G. Woodcock, F. Bittner, T. Mix, K.-H. Müller, S. Sawatzki, O. Gutfleisch, On the reversible and fully repeatable increase in coercive field of sintered Nd–Fe–B magnets following post sinter annealing, J. Magn. Magn. Mater. 360 (2014) 157–164, https://doi.org/10.1016/j.jmmm.2014.02.025.

[48] M. Zakotnik, C.O. Tudor, Commercial-scale recycling of NdFeB-type magnets with grain boundary modification yields products with 'designer properties' that exceed those of starting materials, Waste Manage 44 (2015) 48–54, https://doi.org/10.1016/j.wasman.2015.07.041.

[49] A.S. Kim, Effect of oxygen on magnetic properties of Nd-Fe-B magnets, J. Appl. Phys. 64 (1988) 5571–5573, https://doi.org/10.1063/1.342284.

[50] H. Sepehri-Amin, T. Ohkubo, K. Hono, The mechanism of coercivity enhancement by the grain boundary diffusion process of Nd–Fe–B sintered magnets, Acta Mater. 61 (2013) 1982–1990, https://doi.org/10.1016/j.actamat.2012.12.018.

[51] T. Akiya, T.T. Sasaki, T. Ohkubo, Y. Une, M. Sagawa, H. Kato, K. Hono, The origin of the coercivity reduction of Nd–Fe–B sintered magnet annealed below an optimal temperature, J. Magn. Magn. Mater. 342 (2013) 4–10, https://doi.org/10.1016/j.jmmm.2013.04.044.

[52] J. Li, X. Tang, H. Sepehri-Amin, T. Ohkubo, K. Hioki, A. Hattori, K. Hono, On the temperature-dependent coercivities of anisotropic Nd-Fe-B magnet, Acta Mater. 199 (2020) 288–296, https://doi.org/10.1016/j.actamat.2020.08.040.

[53] F. Vial, F. Joly, E. Nevalainen, M. Sagawa, K. Hiraga, K.T. Park, Improvement of coercivity of sintered NdFeB permanent magnets by heat treatment, J. Magn. Magn. Mater. 242-245 (2002) 1329–1334, https://doi.org/10.1016/S0304-8853(01)00967-2.

[54] B.B. Straumal, Y.O. Kucheev, I.L. Yatskovskaya, I.V. Mogilnikova, G. Schütz, A. N. Nekrasov, B. Baretzky, Grain boundary wetting in the NdFeB-based hard magnetic alloys, J. Mater. Sci. 47 (2012) 8352–8359, https://doi.org/10.1007/s10853-012-6618-5.

[55] A. Yasui, T. Nakamura, Y. Kotani, T. Fukagawa, T. Nishiuchi, S. Hirosawa, Temperature dependence of post-sintered annealing on magnetic properties of intergranular phase in Nd-Fe-B permanent magnet, J. Appl. Phys. 117 (2015), https://doi.org/10.1063/1.4916938.

[56] J. Fidler, T. Schrefl, Overview of Nd–Fe–B magnets and coercivity (invited), J. Appl. Phys. 79 (1996) 5029–5034, https://doi.org/10.1063/1.361565.

[57] M. Huang, Z. Qiu, F. Wang, H. Luo, J. Zhang, High-efficiency utilization of Tb in enhancing the coercivity of Nd-Fe-B magnets by multicomponent Tb70−xPrxCu10Al10Zn10 (x = 0–30) film diffusion, J. Alloys. Compd. 901 (2022) 163619, https://doi.org/10.1016/j.jallcom.2022.163619.

[58] M. Hölscher, D. Raabe, K. Lücke, Rolling and recrystallization textures of bcc steels, Steel Res. 62 (1991) 567–575, https://doi.org/10.1002/srin.199100451.

[59] G. Ding, S. Liao, J. Di, B. Zheng, S. Guo, R. Chen, A. Yan, Microstructure of core-shell NdY-Fe-B sintered magnets with a high coercivity and excellent thermal stability, Acta Mater. 194 (2020) 547–557, https://doi.org/10.1016/j.actamat.2020.05.038.

[60] H. Kronmüller, Theory of Nucleation Fields in Inhomogeneous Ferromagnets, Physica Status Solidi (b) 144 (1987) 385–396, https://doi.org/10.1002/pssb.2221440134.

[61] H. Kronmüller, K.-D. Durst, M. Sagawa, Analysis of the magnetic hardening mechanism in RE-FeB permanent magnets, J. Magn. Magn. Mater. 74 (1988) 291–302, https://doi.org/10.1016/0304-8853(88)90202-8.

[62] T. Helbig, K. Loewe, S. Sawatzki, M. Yi, B.-X. Xu, O. Gutfleisch, Experimental and computational analysis of magnetization reversal in (Nd,Dy)-Fe-B core shell sintered magnets, Acta Mater. 127 (2017) 498–504, https://doi.org/10.1016/j.actamat.2017.01.055.

[63] J. Fischbacher, A. Kovacs, L. Exl, J. Kühnel, E. Mehofer, H. Sepehri-Amin, T. Ohkubo, K. Hono, T. Schrefl, Searching the weakest link: Demagnetizing fields and magnetization reversal in permanent magnets, Scr. Mater. 154 (2018) 253–258, https://doi.org/10.1016/j.scriptamat.2017.11.020.

[64] Y. Li, D. Wu, M. Wang, Z. Wang, W. Liu, Y. Teng, M. Yue, H. Zhang, W. Xia, Magnetization reversal mechanism for core-shell grains in GBD Nd-Fe-B sintered magnets based on in-situ domain observation, J. Alloys. Compd. 906 (2022) 164414, https://doi.org/10.1016/j.jallcom.2022.164414.

[65] D. Givord, M.F. ROSSIGNOL, D.W. TAYLOR, Article, J. Phys. IV France 02 (1992), C3-95-C3-104.

[66] W. Liu, Y. Li, D. Wu, M. Yue, Z. Wang, S. Zha, Y. Liu, X. Yi, Y. Du, Coercivity enhancement mechanism of grain boundary diffused Nd-Fe-B sintered magnets by magnetic domain evolution observation, J. Rare Earths 39 (2021) 682–688, https://doi.org/10.1016/j.jre.2020.05.011.

[67] D. Wu, W.-Q. Liu, M. Yue, Q. Wu, D.-T. Zhang, Q.-M. Lu, X.-L. Li, J.-W. Chen, Coercivity enhancement mechanism of Tb-diffusion Nd–Fe–B sintered magnets studied by magneto-optical Kerr optical microscope, Rare Met 40 (2021) 570–574, https://doi.org/10.1007/s12598-019-01330-2.

[68] N. Oono, M. Sagawa, R. Kasada, H. Matsui, A. Kimura, Production of thick high-performance sintered neodymium magnets by grain boundary diffusion treatment with dysprosium–nickel–aluminum alloy, J. Magn. Magn. Mater. 323 (2011) 297–300, https://doi.org/10.1016/j.jmmm.2010.09.021.

[69] K. Löewe, C. Brombacher, M. Katter, O. Gutfleisch, Temperature-dependent Dy diffusion processes in Nd–Fe–B permanent magnets, Acta Mater. 83 (2015) 248–255, https://doi.org/10.1016/j.actamat.2014.09.039.

[70] C. Lin, S. Guo, W. Fu, R. Chen, D. Lee, A. Yan, Dysprosium diffusion behavior and microstructure modification in sintered Nd-Fe-B magnets via Dual-Alloy method, IEEE Trans. Magn. 49 (2013) 3233–3236, https://doi.org/10.1109/TMAG.2013.2243128.

[71] C.H. de Groot, K.H.J. Buschow, F.R. de Boer, K. de Kort, Two-powder Nd2Fe14B magnets with DyGa-addition, J. Appl. Phys. 83 (1998) 388–393, https://doi.org/10.1063/1.366734.

[72] L. Yuping, W. Mengling, L. Jiayu, Sintered Nd-Fe-B magnet with core–shell structures fabricated through the intergranular addition of ultra-fine as-disproportionated (Nd,Dy)–Fe–B–Cu powder, J Mater Sci: Mater Electron 31 (2020) 7211–7218, https://doi.org/10.1007/s10854-020-03293-y.

[73] K. Opelt, C.-C. Lin, M. Schönfeldt, J. Gassmann, S. Yoon, O. Gutfleisch, Diffusion behavior of heavy rare-earths for grain boundary engineering of sintered Nd-Fe-B-based permanent magnets produced by the 2-powder method, Acta Mater. 270 (2024) 119871, https://doi.org/10.1016/j.actamat.2024.119871.

[74] S. Kim, H.-S. Lee, W.H. Nam, D. Kim, W.H. Shin, J.W. Roh, W. Lee, Enhancement of thermal stability of Nd–Fe–B sintered magnets with tuned Tb-diffused microstructures via temperature control, J. Alloys. Compd. 855 (2021) 157478, https://doi.org/10.1016/j.jallcom.2020.157478.

[75] X.J. Cao, L. Chen, S. Guo, J.H. Di, G.F. Ding, R.J. Chen, A.R. Yan, K.Z. Chen, Improved thermal stability of TbF3-coated sintered Nd–Fe–B magnets by electrophoretic deposition, AIP. Adv. 8 (2018), https://doi.org/10.1063/1.5007099.